FORMATION, CRYSTALLIZATION AND MAGNETIC PROPERTIES OF Nd-Fe-B GLASSES

by

Lexiang Liao

Department of Physics, McGill University

A thesis submitted to the Faculty of
Graduate Studies and Research in partial
fulfillment of the requirements for the
degree of Master of Science

Department of Physics
McGill University
Montreal, Canada
June 1988

摘 要

本工作对金属玻璃 $(Fe_{1-x}Nd_x)_{100-y}B_y$ $(0.025 \le x \le 0.25,$ $5 \le y \le 20)$ 的形成、晶化及其磁性质进行了研究。非晶钕－铁－硼样品是通过快速急冷得到。实验表明对于钕－铁－硼三元合金，当其铁的含量低于 87.5 at% 时，由上述方法可形成非晶相。此类三元非晶合金的热稳定性正比于硼的浓度，但在很大程度上取决于钕与铁的比值。由于铁－硼中少量钕的加入不利于晶化过程中α－铁的形成，从而导致晶化温度随钕的浓度急剧增加。有些成份的合金其晶化产物中含有三元亚稳相。当钕与铁的比值低于 0.176 时，非晶钕－铁－硼合金的居里温度随硼的浓度单调增加；而当钕与铁的比值高于 0.176 时，此居里温度则随硼的浓度增加而单调下降。对所有成份的非晶钕－铁－硼，其本征矫顽力 $(\mu_0 H_c)$ 都小于 0.018 特斯拉；但晶化之后，其矫顽力增加约 50 倍，对不含α－铁的合金尤为如此。

ABSTRACT

The glass formation, crystallization and magnetic properties of $(Fe_{1-x}Nd_x)_{100-y}B_y$ ($0.025 \leq x \leq 0.25$, $5 \leq y \leq 20$) have been investigated. The amorphous Nd-Fe-B alloys were obtained by melt-spinning. The glass formation was found possible for Nd-Fe-B alloys with iron content less than 87.5 at%. The thermal stability of ternary amorphous Nd-Fe-B alloys is proportional to boron concentrations but strongly dependent on Nd:Fe ratio as well. The strong increase of the crystallization temperature with additions of small amounts of neodymium to Fe-B is attributed to the increasing difficulty of α-Fe formation upon crystallization. For some compositions the crystallization products include metastable ternary phases. With increasing Nd:Fe ratio, the increase in Curie temperature of amorphous Nd-Fe-B alloys with boron content is gradually diminished and for Nd:Fe greater than 0.176, even a decrease of Curie temperature with increasing boron content is observed. The intrinsic coercivities of the amorphous Nd-Fe-B alloys was less than 0.018 Tesla for all compositions. After crystallization the coercivities increased by a factor of about 50, specially for alloys free of α-Fe.

RÉSUMÉ

La vitrification, la cristallisation ainsi que les propriétés magnétiques des alliages de $(Fe_{1-x}Nd_x)_{100-y}B_y$ $(0.025 \leq x \leq 0.25,\ 5 \leq y \leq 20)$ ont été étudiées. Les alliages amorphes de Nd-Fe-B ont été obtenus par la méthode du "melt-spinning". La vitrification est possible pour des concentrations de Fe inférieures à 87.5 at%. La stabilité thermique de ces alliages est proportionnelle à la concentration du bore mais dépend aussi au rapport Nd:Fe. La température de cristallisation augmente fortement quand de petites quantités de néodyme sont ajoutées au composé Fe-B. Ce fait est attribué à la difficulté de formation de α-Fe. Pour certaines compositions les produits de cristallisation contiennent des phases ternaires métastables. La température de Curie dans les alliages amorphes de Nd-Fe-B augmente avec la concentration du bore, cependant le taux d'augmentation est graduellement réduit et pour Nd:Fe supérieur à 0.176 une diminution de la température de Curie est observée. La coersivité intrinsèque des alliages amorphes est inférieure à 0.018 Tesla pour toutes les compositions. Après cristallisation la coersivité augmente approximativement par un facteur de 50, surtout pour les alliages ne contenant pas α-Fe.

ACKNOWLEDGEMENTS

I wish, first of all, to thank my supervisor Prof. Zaven Altounian for his guidance, support, encouragement and instruction.

I am very grateful to Prof. Guo-Hua Tu for his help with my experimental work during the period of his one-year visit to McGill.

Thanks are also due to the professors, secretaries and students with whom I am familiar, for their kind help.

I would like to thank the Carl Reinhardt Scholarship for the financial support.

Finally, I am indebted to my wife, Yan Xu, for her many helpful suggestions.

TABLE OF CONTENTS

LIST OF FIGURES

LIST OF TABLES

CHAPTER 1. INTRODUCTION

Recently there has been an upsurge of scientific and technological interest in the new powerful Nd-Fe-B permanent magnet materials discovered by three independent research groups: Sagawa et al., Croat et al. and Koon et al. in 1983<1,2,3>. Apart from the outstanding magnetic properties of Nd-Fe-B magnets, they also have the advantage of relatively low cost of both materials and manufacturing. One can get a clear picture of the discovery of Nd-Fe-B base permanent magnets if one makes the comparison of the Nd-Fe-B materials with several other magnetic materials which have been widely used in modern technology such as telecommunication, data techniques, control devices, motors as well as generators (see table 1.1 <4>).

The development of permanent magnet materials can date back to about the beginning of this century. Magnetic materials giving rise to large hysteresis (high remanence, B_r, and large coercive forces, ${}_BH_c$; see Fig. 1.1 (a)) are commonly described as hard magnetic materials. The remanence B_r determines the flux density which remains after removal of the magnetizing field while the coercive field ${}_BH_c$ is a measure of the material's resistance against demagnetizing fields. One of the most widely applied criteria for the suitability of permanent magnet materials is the maximum energy product $(BH)_{max}$, which is defined as the largest possible value of the product of the flux density B and the corresponding opposing

Table 1.1 Comprision of the magnetic properties of several commercially available permanent magnets

Material	$(BH)_{max}$ (kJm^{-3})	B_r (T)	$_JH_c$ (kAm^{-1})	$_BH_c$ (kAm^{-1})	Price* ($/J)
Ferroxdure 380					
$SrFe_{12}O_{19}$	28.5	0.39	275	265	1
Alnico	83.5	1.04	-	124	2
RES 190					
$SmCo_5$	154	0.89	1100	668	10
REC 26					
$Sm(Co,Fe,Cu,Zr)_7$	215	1.08	800	796	8
Neomax 35					
$Nd_{15}Fe_{77}B_8$	279	1.22	995	891	5

* 1986 prices

Fig. 1.1 a) Comparison of B versus H plots and J versus H plots. The remanence is indicated by B_r and J_r. The corresponding coercive forces are represented by ${}_BH_c$ and intrinsic coercive force ${}_JH_c$, respectively. The flux density B, polarization J and field strength H are related by the equation $B=J+\mu_0H$.

b) Comparison of energy product (BH) corresponding to different working points a,b and c on the B versus H curve.

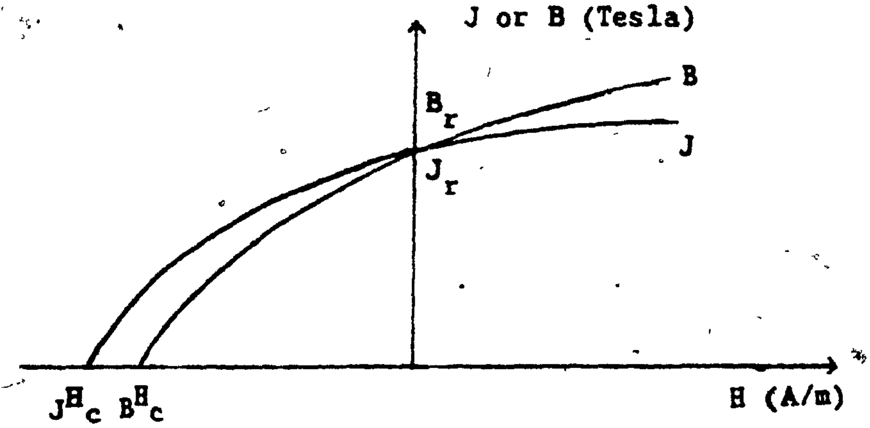
J or B (Tesla)
B
B_r
J
J_r
$_JH_c$
$_BH_c$
H (A/m)

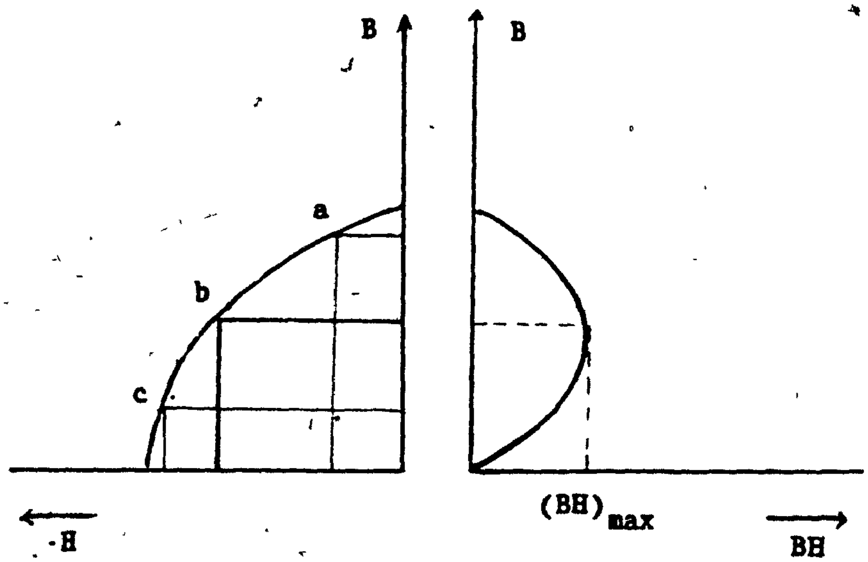
B
B
a
b
c
(BH)max
-H
BH

field H. If the hysteresis loop for a given magnet material is known, it is relatively easy to determine the energy product of a particular magnet body made of this material. This may be illustrated by means of Fig. 1.1b where point (b) on the B-H curve represents the working point of a magnet located at a position where B equals $\mu_0 H$. The energy product corresponding to the point (b) is $(BH)_{max}$.

The carbon steel magnet was first developed at the end of the last century. A substantial improvement came with the appearance of Honda steel in which ~ 35% of the Fe in Fe-W-C steel was substituted by Co. However the high price of Co compared to Fe drove the scientists in the world to explore more powerful permanent magnet materials. The goal was reached in 1936 when the well-known Ticonal II was developed. The considerable freedom in composition and heat treatment of this alloy system called for an optimization of its magnetic properties, which finally led to the appearance of Ticonal XX in 1956. The microstructure of these later magnets was no longer isotropic (as in Ticonal II) but anisotropic which was realized later to be a prerequisite for achieving the high energy products $(BH)_{max}$, in modern permanent magnet materials. The favourable candidates for sufficiently large magnetocrystalline anisotropies are rare-earth base compounds with suitable uniaxial crystal structures, where this property originates from a combination of the crystal-field interaction of the 4f electrons of the rare-earth with the electrostatic charge of the surrounding ions and the relatively strong spin-orbit interaction of the 4f electrons. A sufficiently high magnetization and magnetic ordering temperature is guaranteed by combining rare-earth elements with 3d transition metals. Such a compound which meets all these requirements was discovered in the mid 1960s by K. Strnat et al <5>. They reported that hexagonal RCo_5 (R = Rare earth) compounds of $CaCu_5$ type structure have promising hard magnetic properties. The significant improvement in permanent magnet performance was achieved by using $SmCo_5$. As a matter of fact, $SmCo_5$ was the most powerful magnet material until the discovery of Nd-Fe-B magnets. If the main components of $SmCo_5$ magnets had been cheaper and if there had been a reliable source of Co, the developement of Nd-Fe-B magnets might not have happened or at least been delayed. The 1978 shortage of Co due to political instability in Zaire precipitated a worldwide search for Co-free permanent magnets <6>. This search finally led to the discovery of a new tetragonal phase of composition $R_2Fe_{14}B$.

Besides the powder metallurgical method, an alternate way to prepare the Nd-Fe-B permanent magnet materials is by rapid quenching . In this method, the alloy can be rapidly quenched into an amorphous state and then crystallized by subsequent heat treatment to obtain the optimum magnetic performance by controlling the microstructure. It has already been shown that large coercive forces can be attained which develop either directly during quenching or during subsequent crystallization <7,8,9>. The origin of coercive forces was attributed to the formation of metastable or nonequilibrium phases in conjunction with finely divided microstructure, which under optimum conditions can approach the single-domain critical size (single-domain particle diameter ~ 150nm for melt-spun materials <2>). In addition, the rapid quenching methods offer the possibility of preparing metastable compounds not obtainable by either powder metallurgy or liquid-phase sintering. Therefore, when these methods are used, the chance of finding novel materials is considerably increased and improvements of hard magnetic properties of materials is simply achieved by controlled addition of selected elements to Nd-Fe-B.

As mentioned above, when the rapid quenching methods are employed for preparing permanent magnet materials, the alloy is first required to be quenched into an amorphous state. So called amorphous metallic alloys, which also have been called glassy alloys or non-crystalline alloys, are metal alloys with no long range atomic order. The absence of long range atomic order induces many unique properties for amorphous materials. For example, they behave as very soft magnetic materials; mechanicallly, they are exceptionally hard and have extremely high tensile strengths; and some of them are excellent corrosion resistant. These unique properties have stimulated a huge amount of investigations into the amorphous materials since Duwez and his cowokers discovered a method of preparing amorphous alloys by direct quenching from the melt in 1960's <10>. It has been demonstrated that most of binary alloys such as the transtion metal-metalloid type (TM-M) and the rare-earth-transition metal (RE-TM), are good glass forming systems.

So far, although a lot of work has been done on the crystallographic and magnetic properties of Nd-Fe-B base alloys, the glass forming ability of the ternary Nd-Fe-B system and the magnetic and thermal properties of amorphous Nd-Fe-B alloys have been the subjects of relatively very few investigations. The first report of magnetic properties of amorphous iron-rare-earth-boron alloys was made by S.H. Aly et al. <11>. They studied the magnetic properties of melt-spun $Fe_{77}R_{15}B_8$ amorphous alloys with R = Y, La, Pr, Nd, Sm, Gd, Tb, Dy and Er in the temperature range 4.2-800K. The magnetic ordering temperatures of these alloys were found to be in the range 360-570K and are well below the crystallization temperatures. More attention to amorphous alloys in the Nd-Fe-B system was paid by Buschow et al. <12>. They have studied the crystallization behaviour of some amorphous alloys of iron-rich composition in the Nd-Fe-B system and found that the thermal stability of the alloys increases with boron concentrations, while increasing the neodymium concentration gives rise to a strong initial increase in the thermal stability but leads to a decrease at higher neodymium concentrations. The varation of the thermal stability of Nd-Fe-B amorphous alloys cannot be understood by their work.

As we know, a controlled crystallization of the melt-spun materials controls the microstructure and therefore is a prerequiste for the attainment of sufficiently large coercive forces. It is therefore of significance to understand the glassy forming ability and thermal stability of ternary Nd-Fe-B system. To avoid unnecessary grain growth of the $Nd_2Fe_{14}B_1$ phase, all high performance magnets <2> always have an off-stoichometric composition. It is therefore necessary to determine the nature and the role of grain boundary phase or phases around the tetragonal hard magnetic phase. Crystallization studies of the amorphous Nd-Fe-B alloys provide a direct determination of these phases and a crystalline ternary phase diagram can be established in the region of interest. In addition, very little is known about the magnetic properties of the amorphous Nd-Fe-B alloys. Based on these reasons, we pursue a systematic study of the formation and crystallization of the iron-rich corner of the ternary Nd-Fe-B amorphous alloys.

In the next chapter, a description of the preparation of melt-spun alloys $(Fe_{1-x}Nd_x)_{100-y}B_y$ ($0.025 \leq x \leq 0.25$, $5 \leq y \leq 20$) and experimental methods used in this study will be given. The experimental results and discussions will be presented in the third chapter. The last chapter gives the main conclusions derived from this work.

CHAPTER 2. EXPERIMENTAL METHODS

This chapter describes the experimental methods used in sample preparation and measurements. A detailed description of sample preparation is presented in the first section. The section for sample measurements includes a brief description of the various instruments used, such as differential scanning calorimeter (DSC), X-ray diffractometer and vibrating sample magnetometer (VSM).

2.1. Sample Preparation

The $(Fe_{1-x}Nd_x)_{100-y}B_y$ alloys were prepared by induction melting appropriate amount of 99.99% pure Fe, 99.9% pure Nd and 99.9% pure B on a water-cooled copper boat under titanium gettered argon(see Fig. 2.1 for a schematic diagram). It was found that this method can produce much cleaner samples than conventional arc-melting. In order to ensure homogeneity, each alloy button (about 2g) was melted up to five times. Sample mass losses were essentially less than 0.4 mg after five melts. Glassy ribbons were obtained by melt spinning under Ar atmosphere instead of He. It was found, experimentally, that Ar atmosphere increased the contact time of the ribbon with the wheel because of the higher viscosity coefficient of Ar. The molten alloy was ejected by argon pressure through a small orifice of size 0.4 mm at the bottom of a quartz crucible onto the surface of the

Fig. 2.1 A schematic digram of the water-cooled copper boat

1. to rf power supply
2. sample
3. cooling water inlet
4. vacuum pump
5. quartz tube
6. cooling water outlet.
7. Ar gas
8. titanium .
9 and 10. valves
11 and 12. pressure gauges
13. copper boat

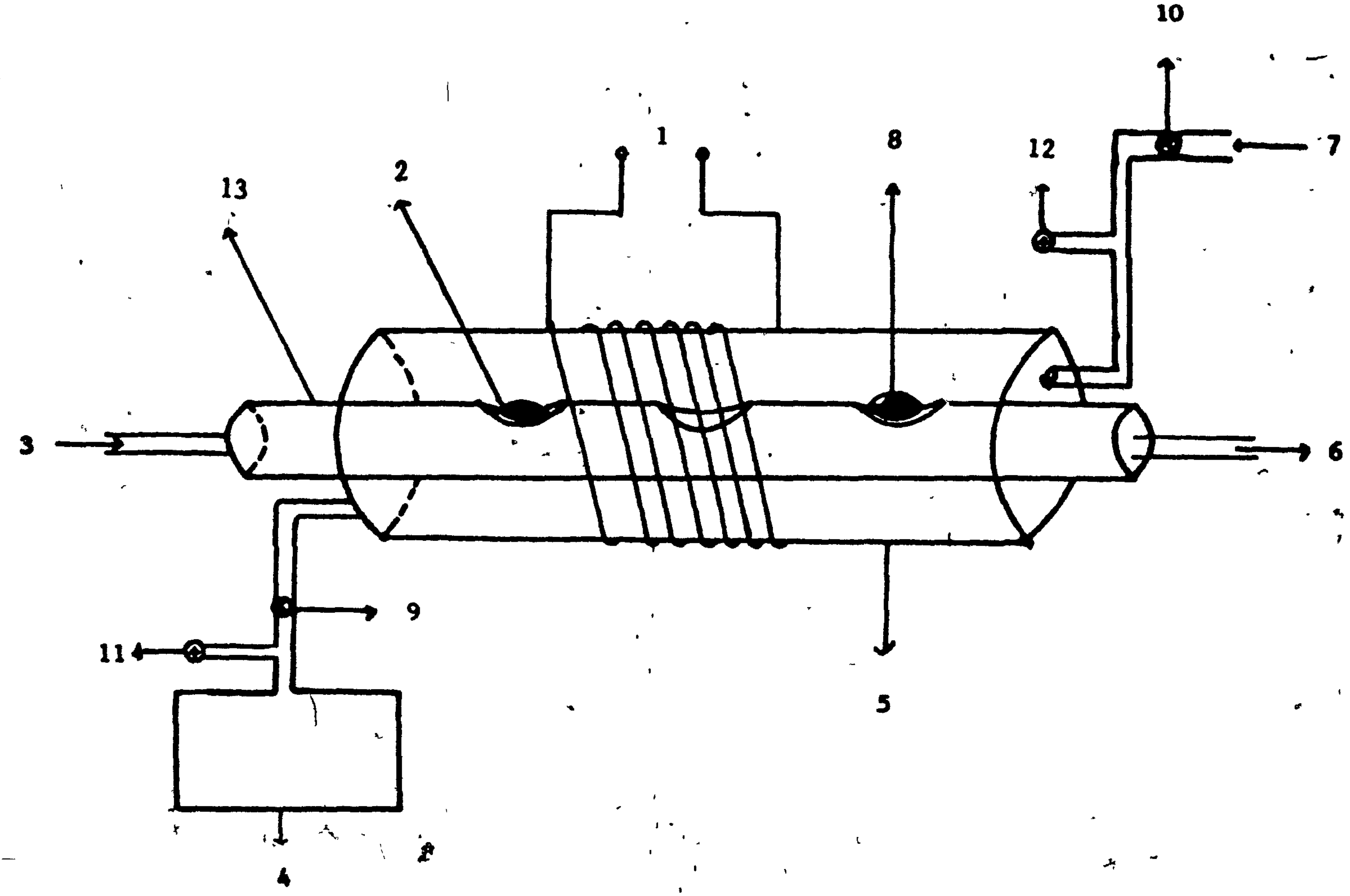10
1
8
12
7
13
2
3
6
9
11
5
4

rotating steel wheel. Experiments showed the quality of ribbon sample could be greatly improved by using a steel wheel instead of the more common copper wheel, since samples with high iron content the differential thermal contraction after solidification is smaller with the steel wheel than with the copper wheel. The tangential speed of the wheel was kept at 45 m/s. The glassy ribbons were typically 1-2 mm wide and 20-30 μm thick. The brittleness of the ribbons increased with neodymium content. X-ray diffractometer scans did not show any sign of crystallinity for most of the samples used in this study. Only a few alloys with iron content greater than 87.5 at% Fe showed some low intensity Bragg reflections characteristic of a partially crystalline alloy. Fig. 2.2 shows the X-ray diffraction pattern of a typical amorphous ribbon of the ternary Nd-Fe-B alloys.

2.2 Measurements

2.2.1 Differential Scanning Calorimeter (DSC)

A very essential tool for studying thermal properties of metallic glasses is the DSC (see Fig. 2.3 for a schematic diagram of Perkin Elmer DSC-IIc). Here the sample, enclosed in a small Al or Au pan, and an empty reference pan are subjected to identical thermal programmes and the difference in heat flow between the two is monitored by a thermometer through a feedback system. The normal way to measure the thermal properties in the DSC is to heat the amorphous sample under a flow of

Fig. 2.2 A typical X-ray diffraction pattern of an amorphous Nd-Fe-B alloy taken with CuKα radiation

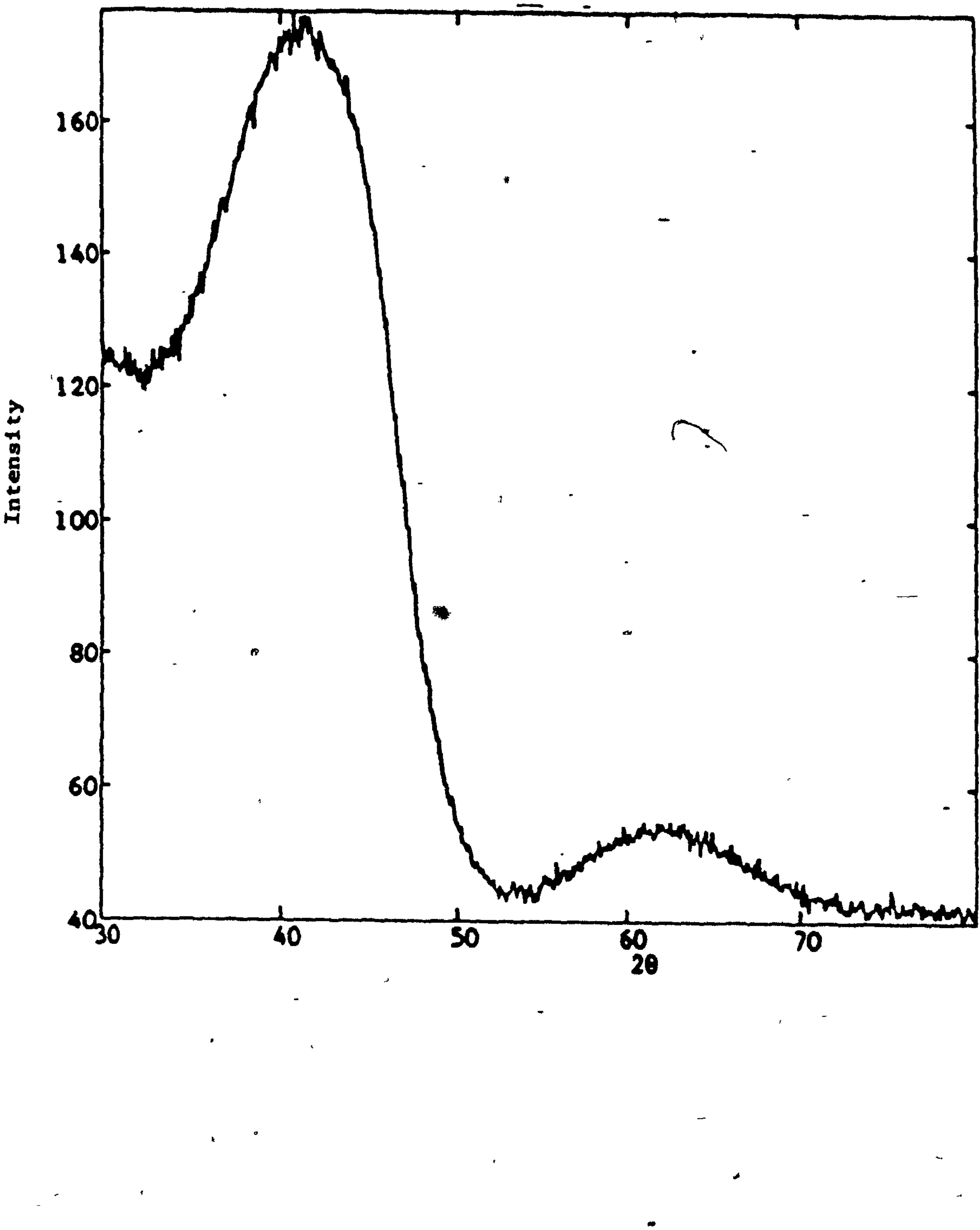
Intensity
160
140
120
100
80
60
40
30
40
50
60
70
2θ

Fig. 2.3 A schematic diagram of Perkin Elmer DSC-IIc

1. sample holder
2. reference holder
3. resistance thermometer
4. heater
5. argon inlet
6. argon outlet
7. aluminum body (heat-sink)
8. thermometer for sample and reference
9. power supplies for sample and reference heater
10. sample confined in aluminum pan or gold pan
11. reference container (empty aluminum pan or gold pan)

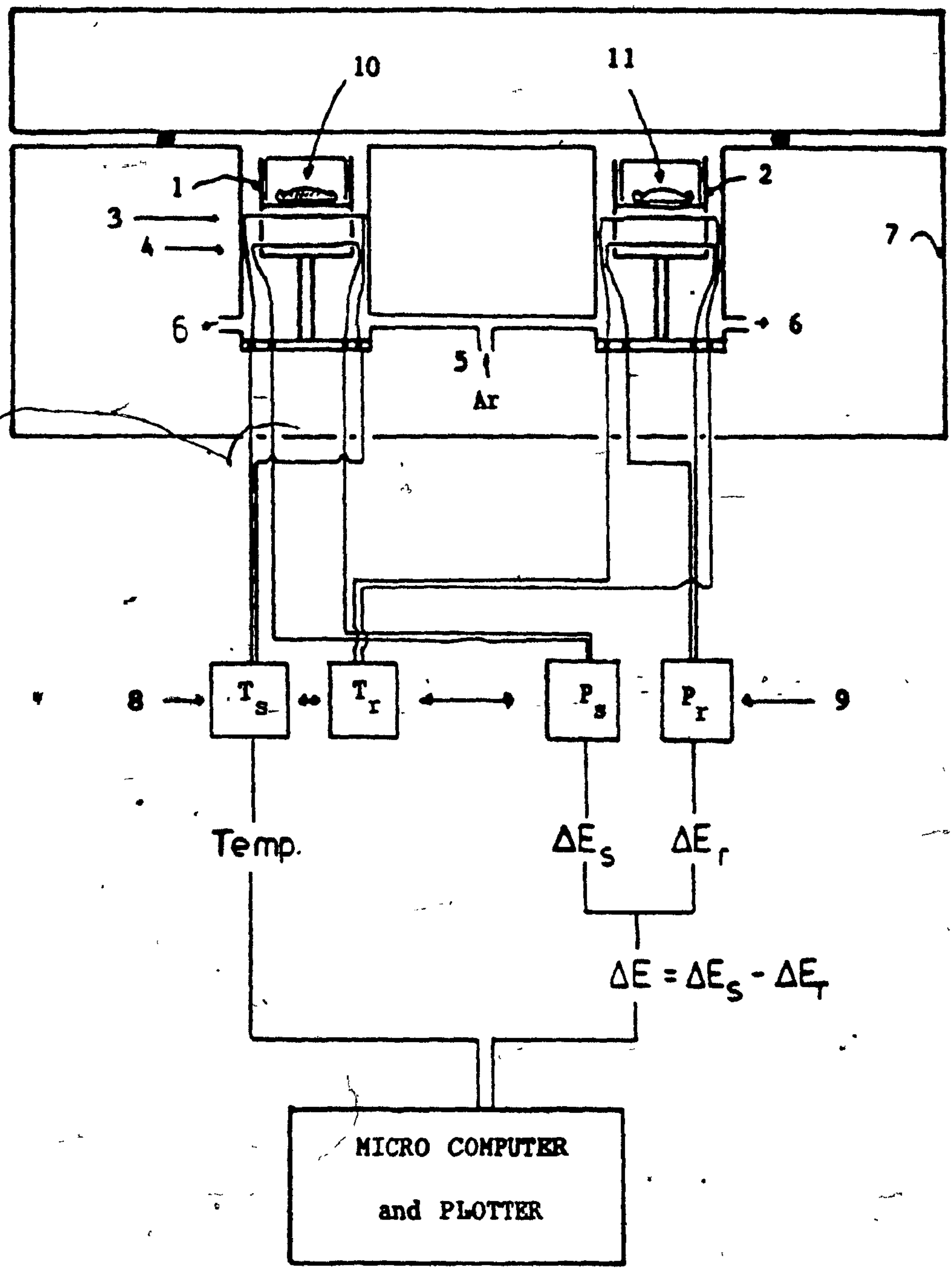
10
11
1
2
3
4
7
6
6
5
Ar
8
T_s
T_r
P_s
P_r
9
Temp.
ΔE_s
ΔE_r
$\Delta E = \Delta E_s - \Delta E_r$
MICRO COMPUTER
and PLOTTER

oxygen-free argon gas at a constant heating rate. The thermogram is recorded via a computer. A typical thermogram observed in the present study is shown in Fig. 2.4. The small endothermic "kink" in the curve (a) is due to the magnetic ordering temperature. The DSC, therefore, can be used to determine the Curie temperature, T_c of magnetic materials. The large exothermic peak in the curve (b) is due to the crystallization of the amorphous sample.

The dependence of the crystallization temperature (T_x) , defined at the peak of the exotherm, on heating rate ϕ can be used to obtain an activation energy for crystallization. In the method proposed by Kissinger <13>, $\ln\frac{\phi}{T_x^2}$ is plotted against $\frac{1}{T_x}$, the slope of the resulting straight line gives the activation energy. Fig. 2.5 shows Kissinger plots for the samples containing 12.5 at% B.

2.2.2 X-ray diffraction

X-ray diffraction is a well-known technique for studying the structure of a material. It can be used not only to identify the crystalline phases of alloys but also to verify the amorphous nature of the alloys. The X-ray diffraction measurements was done in the reflection mode with monochromatic copper $K\alpha_1$ radiation (wavelength 1.54056 Å). Fig. 2.6 shows the schematic diagram of the X-ray diffractometer. The diffractometer used in this study was an automated Nicolet-Stöe L11 powder diffractometer. The ribbon

Fig. 2.4 DSC curve for alloy $Nd_{12}Fe_{68}B_{20}$

a). Curie temperature curve obtained by heating the amorphous alloy at a rate of 80 K/min

b). crystallization exotherm at 40 K/min

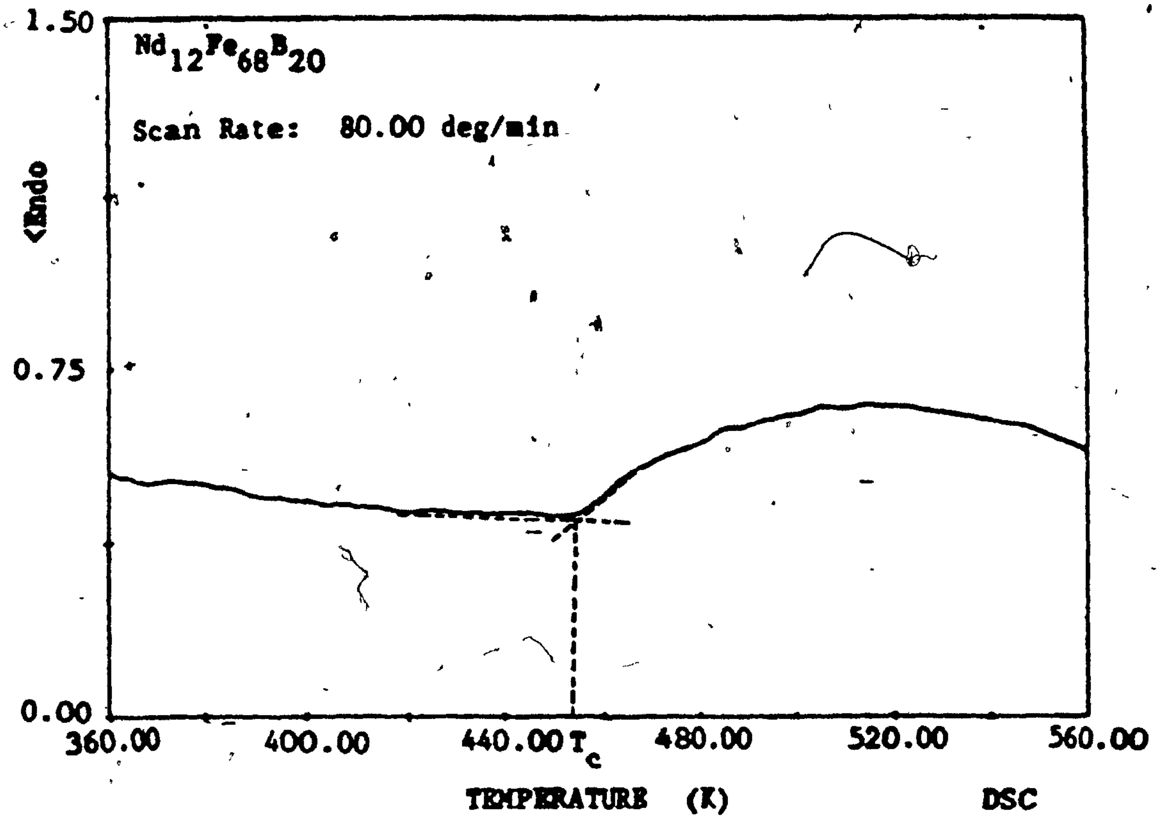
$Nd_{12}Fe_{68}B_{20}$
Scan Rate: 80.00 deg/min
<Endo
1.50
0.75
0.00
360.00
400.00
440.00
T_c
480.00
520.00
560.00
TEMPERATURE (K)
DSC

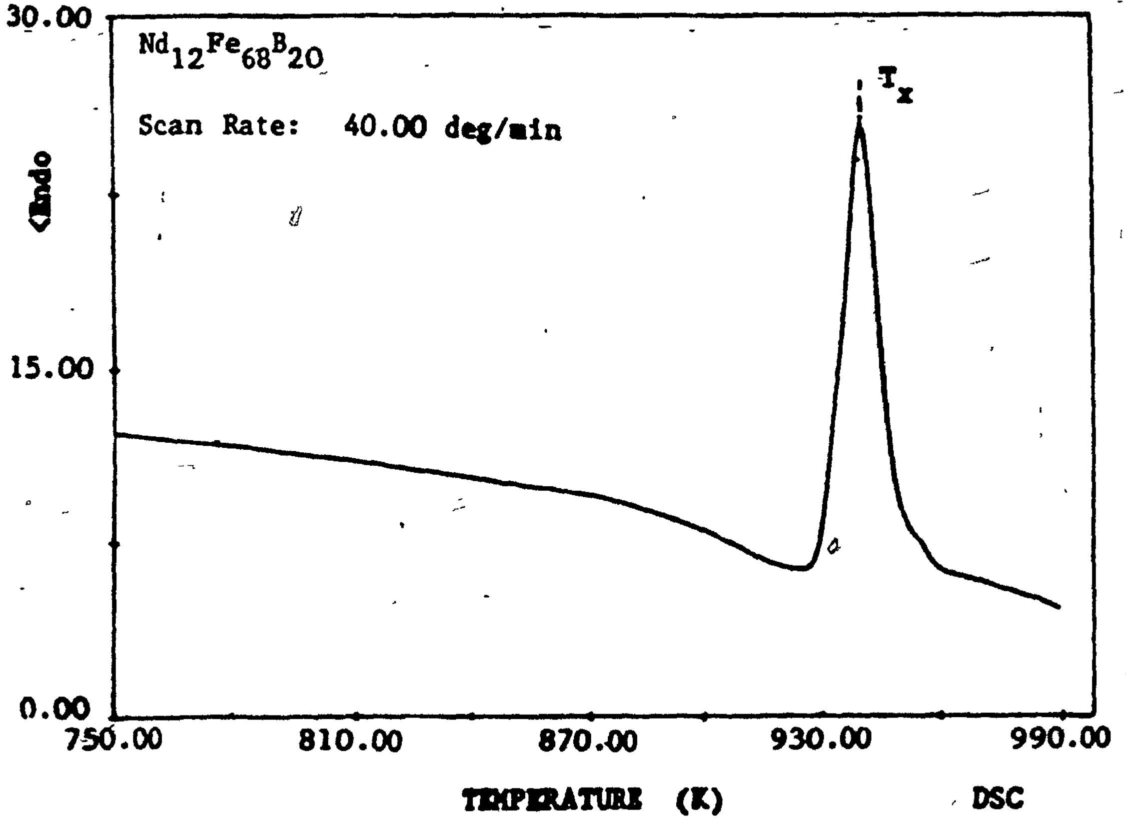
$Nd_{12}Fe_{68}B_{20}$
Scan Rate: 40.00 deg/min
<Endo
T_x
30.00
15.00
0.00
750.00
810.00
870.00
930.00
990.00
TEMPERATURE (K)
DSC

Fig. 2.5 Kissinger plots for alloys with composition $(Fe_{1-x}Nd_x)_{87.5}B_{12.5}$

KISSINGER PLOTS

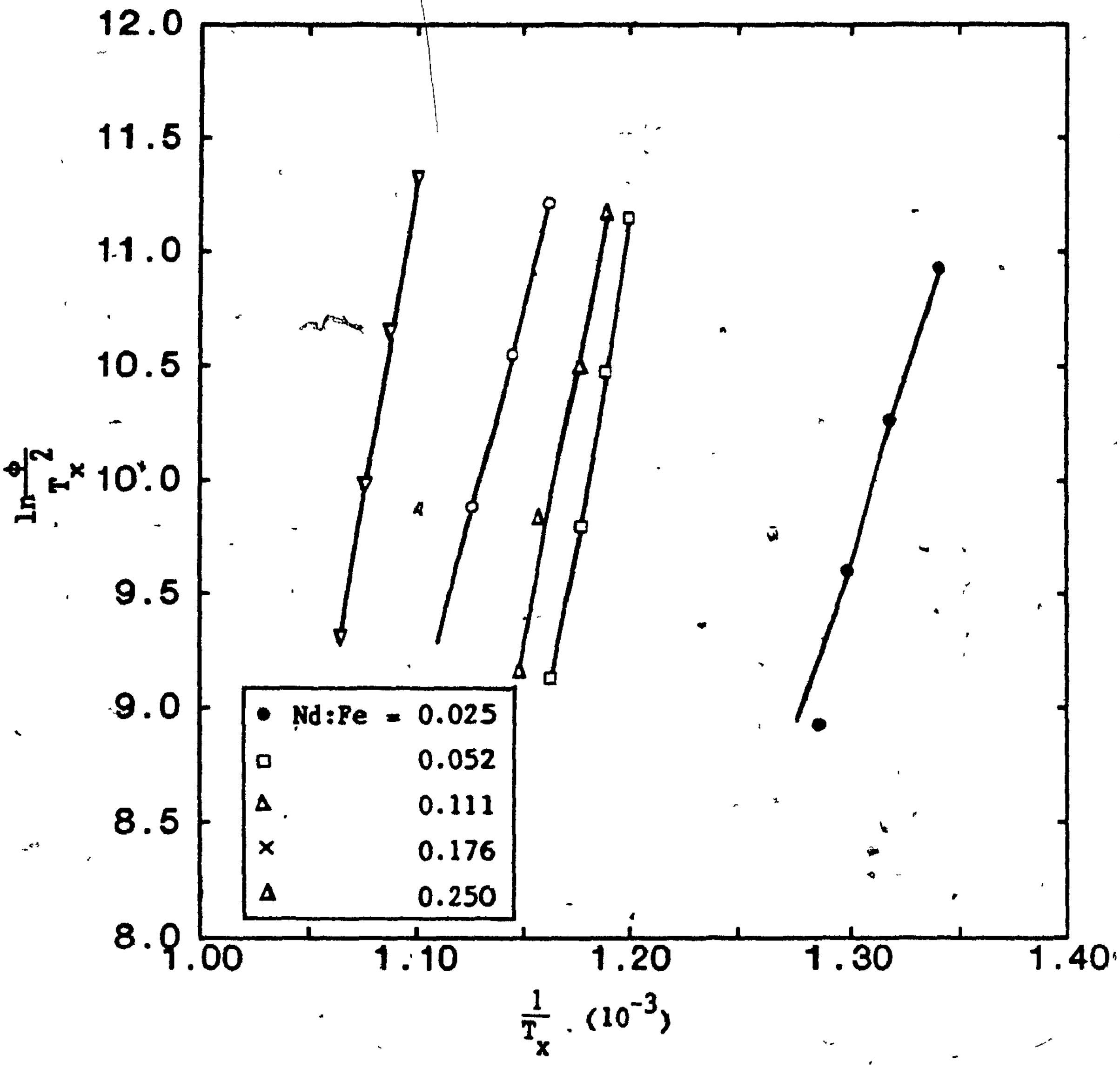

Fig. 2.6 A schematic diagram of the X-ray diffractometer

1. X-ray tube
2. anode
3. X-ray source slit
4. sample holder and sample
5. monochromator
6. detector
7. analizer slit

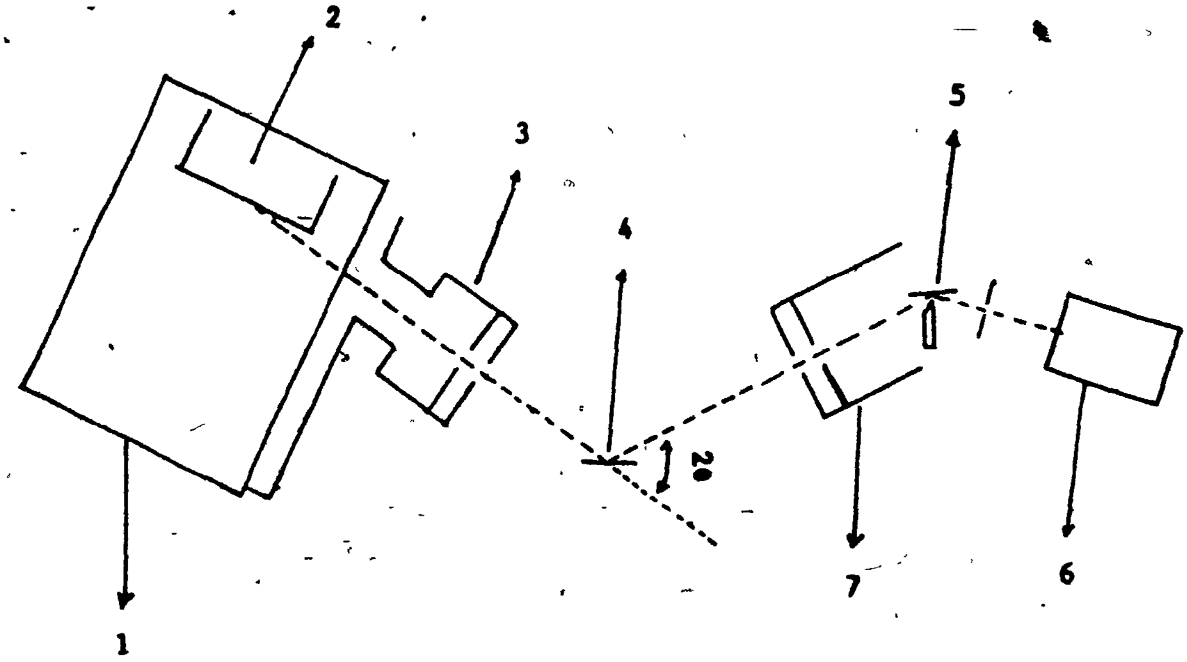
2
3
4
5
2θ
1
7
6

samples were mounted on a thin glass plate using a double sided adhesive tape. To test for amorphousness, 2θ diffraction scans were made in the range 30° to 50°. The step size and exposure time were 0.1° and 20 seconds respectively. To obtain the X-ray diffraction pattern for the recrystallized alloys free of texturing effects, the ribbon samples were first powdered and 2θ diffraction scans were taken in the range 25° to 70°. The step size and exposure time were 0.1° and 40 seconds respectively. A representative X-ray diffraction spectrum for an alloy after crystallization is displayed in Fig. 2.7.

2.2.3 Vibrating Sample magnetometer (VSM)

Magnetization measurements were performed at room temperature in a Foner-type vibrating sample magnetometer (see Fig. 2.8 for a schematic diagram of VSM). In this technique, the sample vibrates in a vertical direction in a horizontal applied DC magnetic field and the AC signal induced by the dipole field of the sample in a pair of secondary coils placed on both sides of the sample is amplified and compared with a signal produced by a standard magnet, giving rise to an output signal which is directly proportional to the magnetic moment of the sample. The sample is magnetized by the applied DC magnetic field of up to 1.7T. The hysteresis loop is plotted on the X-Y recorder. The samples (~ 5mg) for magnetization measurement were prepared by using epoxy resin to hold the ribbon fragments.

Fig. 2.7 A representative X-ray diffraction spectrum for the amorphous alloy after crystallization. The broad peak around 21° is due to the glass substrate.

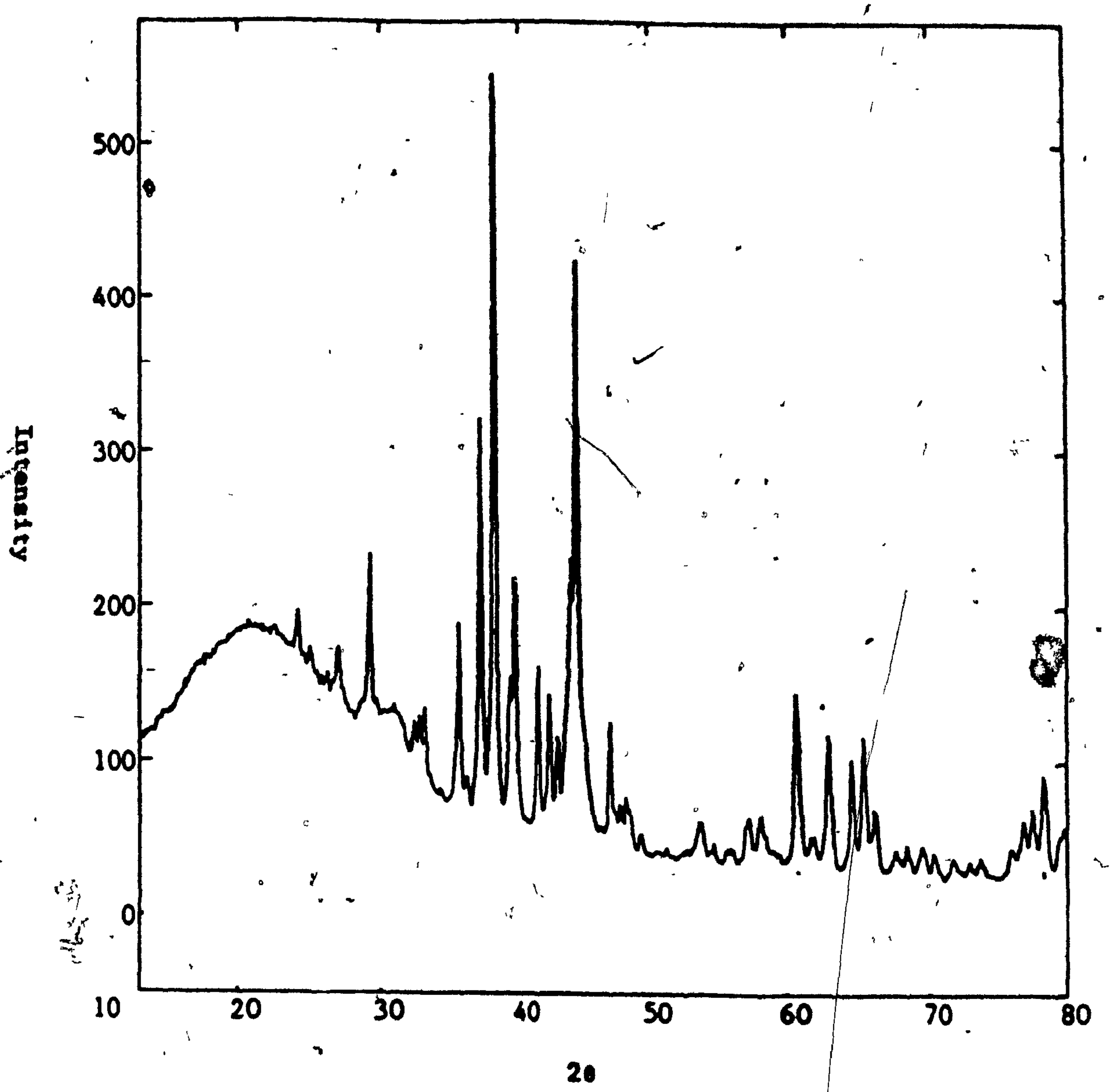

Intensity
500
400
300
200
100
0
10
20
30
40
50
60
70
80
2θ

Fig. 2.8 A schematic diagram of VSM

1. signal pick-up coil for standard magnet
2. standard magnet
3. DC magnetic field
4. signal pick-up coil for sample
5. sample holder
6. X-Y recorder
7. lock-in amplifier
8. loud - speaker transducer

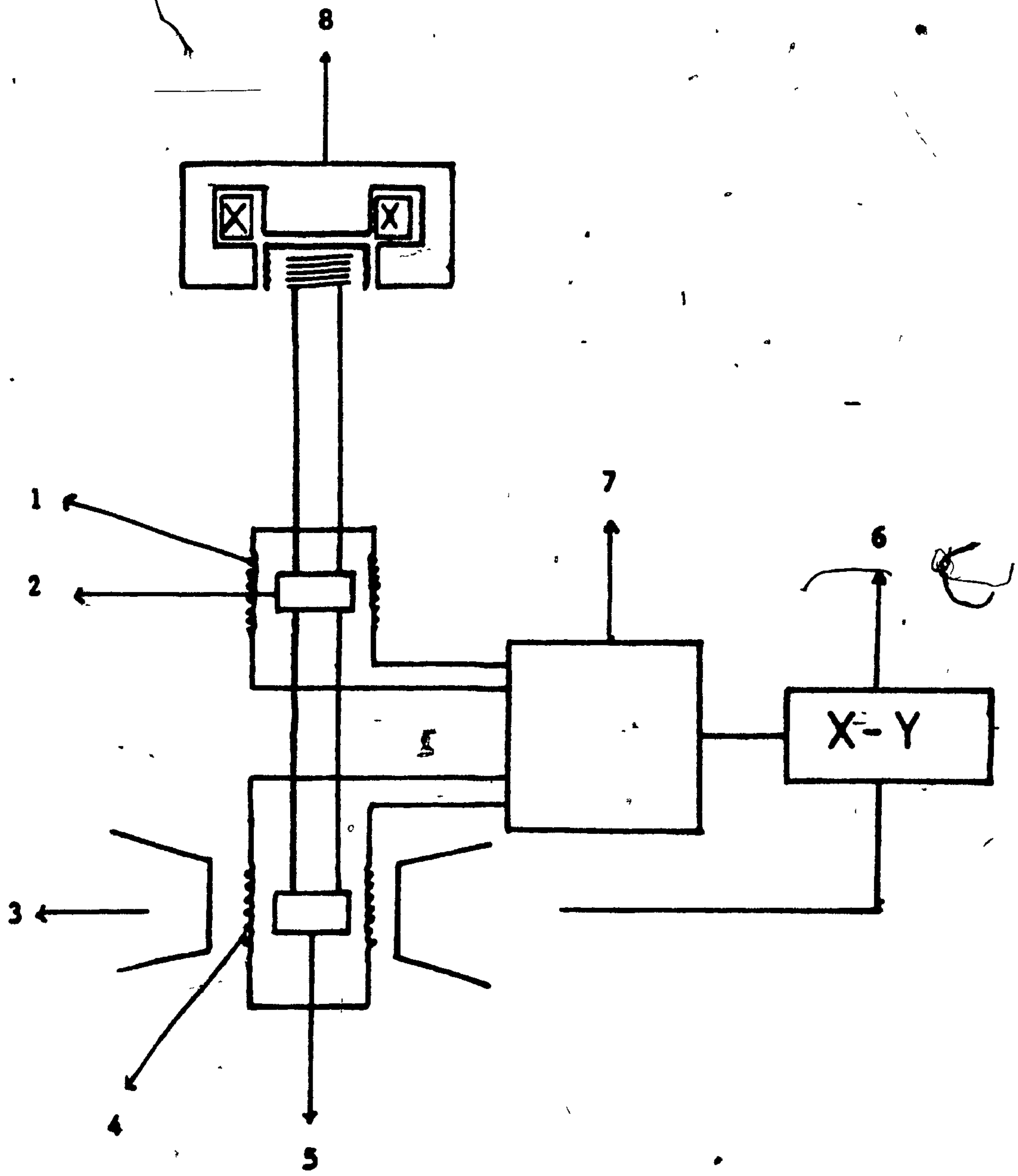
8
1
2
7
6
X-Y
3
4
5

CHAPTER 3. EXPERIMENTAL RESULTS AND DISCUSSIONS

The experimental results are presented and discussed in this chapter. First a description will be given of the glass formation for the Fe-rich corner of the ternary Nd-Fe-B system. The behaviour of crystallization temperature for such ternary amorphous alloys will be described and discussed in terms of their concentration dependence in section 3.2. The last part of this chapter will be devoted to the magnetic properties of the ternary Nd-Fe-B alloys.

3.1 Glass Forming Ranges in the Ternary Nd-Fe-B System

The ranges for glass formation for the alloys $(Fe_{1-x}Nd_x)_{100-y}B_y$ were investigated by means of X-ray diffraction. The amorphous nature of the samples was verified with featureless X-ray spectra, except a broad maximum centered around $2\theta \approx 44°$. Fig. 3.1 indicates the ranges for glass formation for the Fe-rich corner of the ternary Nd-Fe-B system. The dashed line in Fig. 3.1 means that compositions richer in B were not fully investigated for glass forming ability whereas the solid line gives the critical composition boundary for glass formation. The results show that increasing neodymium content (≥ 20 at%) or decreasing boron content (≤ 7.5 at%) makes it more difficult to prepare amorphous samples.

Fig. 3.1 Ranges for glass formation for Fe-rich corner in the ternary Nd-Fe-B system

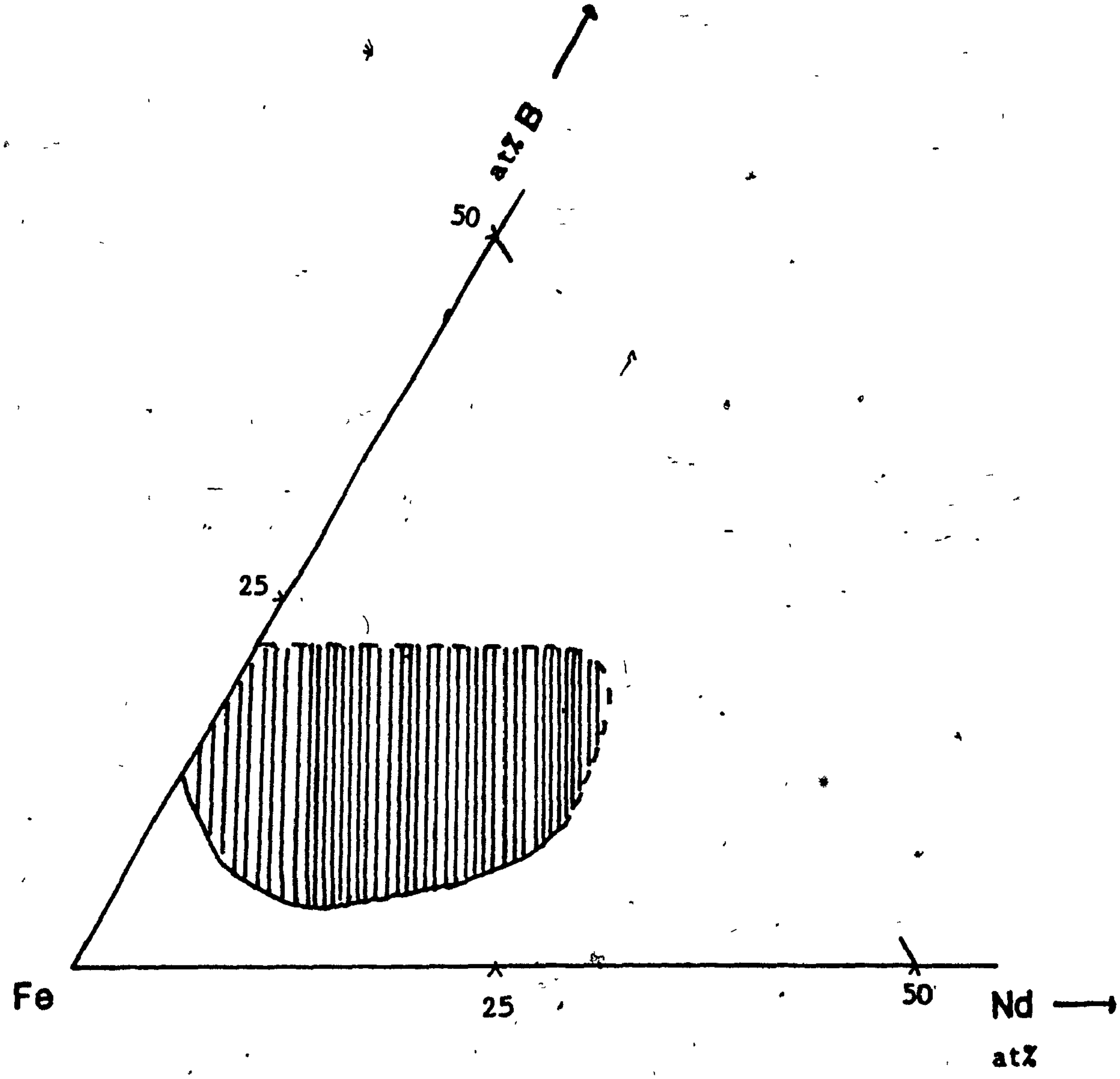
at% B
50
25
Fe
25
50
Nd
at%

3.2 Crystallization Behaviour of Amorphous $(Fe_{1-x}Nd_x)_{100-y}B_y$ Alloys

3.2.1 Concentration Dependence of Crystallization Temperature

Some typical results obtained by DSC measurements are shown in Fig. 3.2. In some of the amorphous alloys, such as $(Fe_{1-x}Nd_x)_{87.5}B_{12.5}$ with x = 0.200 and 0.250, there was only a single crystallization exotherm, in other alloys the crystallization process is more complex and more than one exotherm was observed. For example, in the alloys $(Fe_{1-x}Nd_x)_{87.5}B_{12.5}$ with x = 0.050, 0.100 and 0.150, there were two exotherms whereas in the alloy $(Fe_{0.975}Nd_{0.025})_{87.5}B_{12.5}$ even three exotherms were observed (see Fig. 3.2). The crystallization temperature (T_x) corresponding to the peak of the lowest exotherm are designated T_1, those corresponding to higher temperature are designated T_2 or T_3. The results of T_1, T_2 and T_3 obtained with a heating rate of 40 K/min are collected in tables 3.1 - 3.6. A dash in the tables indicates the absence of higher temperature exotherms in the temperature range (320 ~ 1000K) considered in the present study.

Fig. 3.3 shows the first crystallization temperature, T_1, as a function of boron concentration. It can be seen from Fig. 3.3 that T_1 increases steadily with boron concentration while the Nd:Fe ratio was kept constant. The maximum variation of about 100K for the first crystallization temperature (T_1) in the range of 5 - 20 at% B was obtained for alloys with Nd:Fe = 0.111 whereas the minimum variation of about 50K

Fig. 3.2 DSC traces of amorphous $(Fe_{1-x}Nd_x)_{87.5}B_{12.5}$ alloys obtained with a heating rate of 40 K/min

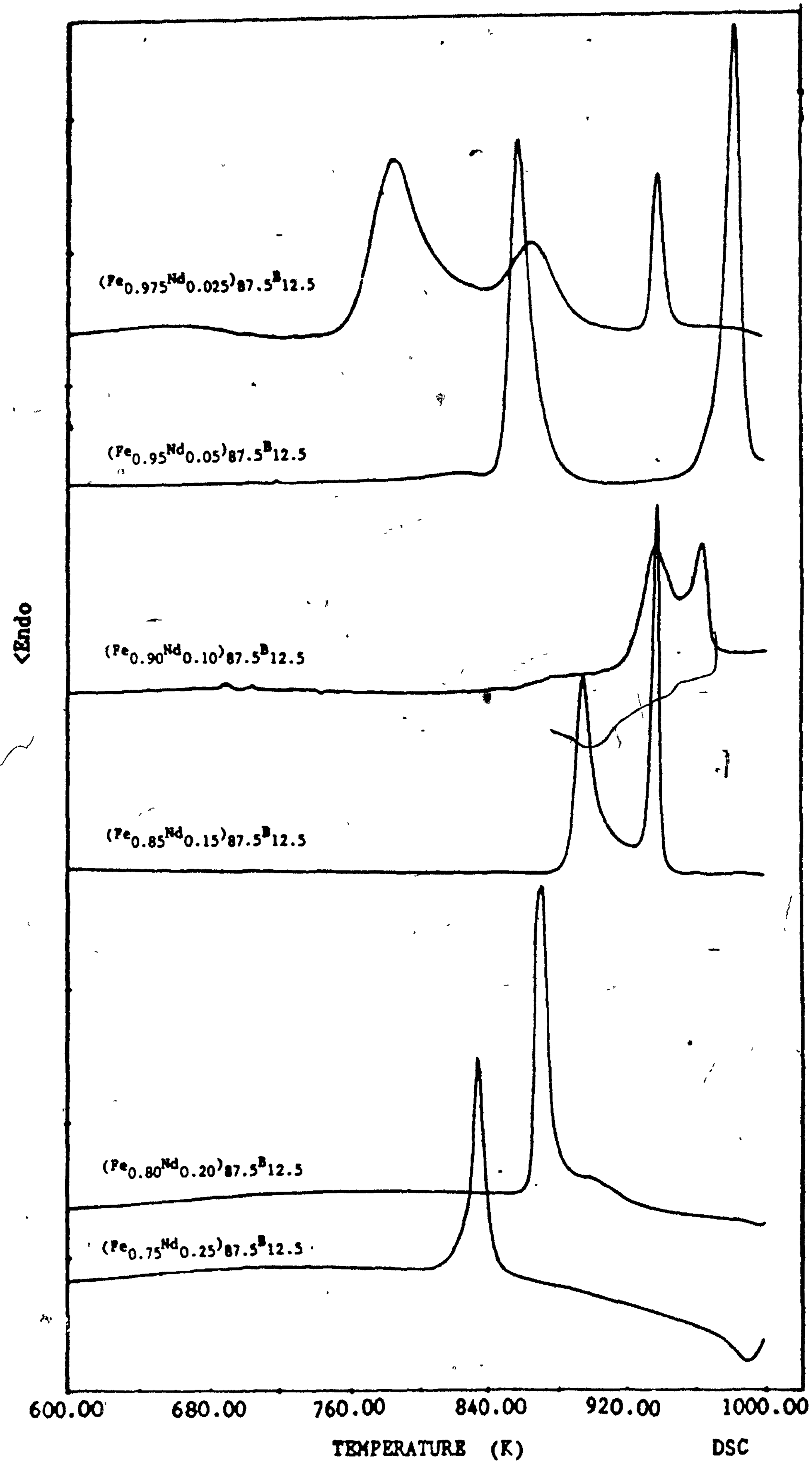
(Fe$_{0.975}$Nd$_{0.025}$)$_{87.5}$B$_{12.5}$
(Fe$_{0.95}$Nd$_{0.05}$)$_{87.5}$B$_{12.5}$
(Fe$_{0.90}$Nd$_{0.10}$)$_{87.5}$B$_{12.5}$
(Fe$_{0.85}$Nd$_{0.15}$)$_{87.5}$B$_{12.5}$
(Fe$_{0.80}$Nd$_{0.20}$)$_{87.5}$B$_{12.5}$
(Fe$_{0.75}$Nd$_{0.25}$)$_{87.5}$B$_{12.5}$
<Endo
600.00
680.00
760.00
840.00
920.00
1000.00
TEMPERATURE (K)
DSC

Table 3.1 Curie temperature (T_c) obtained at a heating rate of 80 K/min and crystallization temperature of the first (T_1), second (T_2) and third (T_3) obtained at a heating rate of 40 K/min and the corresponding crystalline phases in $(Fe_{0.975}Nd_{0.025})_{100-y}B_y$

y	T_c (K)	T_1 (K)	E_{1a} (ev)	Crystalline Phases	T_2 (K)	Crystalline Phases	T_3 (K)	Crystalline Phases
5	393.5*	-			-		-	
7.5	411.5*	-			-		-	
10	442.6	742.3		α-Fe	871.8	α-Fe Fe_3B $Nd_{1.1}Fe_4B_4$	932.1	α-Fe Fe_3B $Nd_{1.1}Fe_4B_4$
12.5	499.5	776.8	2.8	α-Fe	857.9	α-Fe Fe_3B (900K)	931.2	α-Fe Fe_3B $Nd_{1.1}Fe_4B_4$
15	533.7	796.4		α-Fe	829.6	α-Fe Fe_3B (900K)	926.0	α-Fe Fe_3B $Nd_{1.1}Fe_4B_4$
20	601.5	828.1		α-Fe $Nd_{1.1}Fe_4B_4$	-		-	

* α-Fe phase was observed in the X-ray diagrams of these as-spun sample

Table 3.2 As table 3.1, but for $(Fe_{0.95}Nd_{0.05})_{100-y}B_y$

y	T_c (K)	T_1 (K)	E_{1a} (ev)	Crystalline Phases	T_2 (K)	Crystalline Phases
5	367.5*	835.7		α-Fe $Nd_2Fe_{14}B_1$ $Nd_{1.1}Fe_4B_4$	-	
7.5	407.5	832.4		α-Fe $Nd_2Fe_{14}B_1$ (870K)	903.6	α-Fe $Nd_2Fe_{14}B_1$ $Nd_2Fe_{14}B_1$
10	438.7	836.8		New-Phase α-Fe (900K)	954.6	α-Fe $Nd_2Fe_{14}B_1$ $NdFe_{12}B_6$
12.5	488.1	850.2	4.87	New-Phase α-Fe (900K)	974.5	α-Fe $Nd_2Fe_{14}B_1$ $NdFe_{12}B_6$
15	520.4	860.2		New-Phase α-Fe (900K)	-	α-Fe $Nd_2Fe_{14}B_1$ $Nd_2Fe_{23}B_3$
17.5	535.3	865.9		α-Fe Fe_3B (910K)	931.2	α-Fe $Nd_2Fe_{14}B$ Fe_3B
20	563.5	874.3		α-Fe Fe_3B (910K)	930.7	α-Fe $Nd_2Fe_{14}B_1$ Fe_3B

Table 3.3 As table 3.1, but for $(Fe_{0.90}Nd_{0.10})_{100-y}B_y$. The last column gives the intrinsic coercivities for the crystallized alloys.

y	T_c (K)	T_1 (K)	E_{1a} (ev)	Crystalline Phases	T_2 (K)	Crystalline Phases	$\mu_0 {}_JH_c$ (T)
5	395.1	867.6		α-Fe $Nd_2Fe_{14}B_1$ α-Nd	-		0.4
7.5	443.5	869.9		α-Fe $Nd_2Fe_{14}B_1$ $Nd_{1.1}Fe_4B_4$	-		0.57
10	455.4	896.8		α-Fe $Nd_2Fe_{14}B_1$ $Nd_{1.1}Fe_4B_4$	-		0.4
12.5	501.5	928.4	6.45	$Nd_2Fe_{14}B_1$ $Nd_2Fe_{23}B_3$ (950K)	954.1	α-Fe $Nd_2Fe_{14}B_1$ $Nd_{1.1}Fe_4B_4$	0.25
15	490.4	955.5		$Nd_2Fe_{14}B_1$ $Nd_2Fe_{23}B_3$ $Nd_{1.1}Fe_4B_4$	-		0.23
17.5	494.3	966.6		$Nd_2Fe_{14}B_1$ $Nd_2Fe_{23}B_3$ $Nd_{1.1}Fe_4B_4$	-		0.15
20	499.3	962.7		α-Fe $Nd_2Fe_{14}B_1$ $Nd_2Fe_{23}B_3$ $Nd_{1.1}Fe_4B_4$	967.7		0.05

Table 3.4 As table 3.3, but for $(Fe_{0.85}Nd_{0.15})_{100-y}B_y$

y	T_c (K)	T_1 (K)	E_{1a} (ev)	Crystalline Phases	T_2 (K)	Crystalline Phases	$\mu_0\,{}_JH_c$ (T)
5	389.7	859.7		α-Fe $Nd_2Fe_{14}B_1$ α-Nd	-		0.55
7.5	430.3	864.5		α-Fe $Nd_2Fe_{14}B_1$ α-Nd	-		1.20
10	446.4	882.3		$Nd_2Fe_{14}B_1$	929.1	$Nd_2Fe_{14}B_1$ $Nd_{1.1}Fe_4B_4$ α-Nd	1.34
12.5	452.7	887.6	3.30	$Nd_2Fe_{14}B_1$	929.4	$Nd_2Fe_{14}B_1$ $Nd_{1.1}Fe_4B_4$ α-Nd	1.13
15	450.7	906.7		$Nd_2Fe_{14}B_1$ $Nd_{1.1}Fe_4B_4$	928.6	$Nd_2Fe_{14}B_1$ $Nd_{1.1}Fe_4B_4$	0.58
17.5	448.3	941.8		$Nd_2Fe_{14}B_1$ $Nd_{1.1}Fe_4B_4$ $NdFe_{12}B_6$	-	–	0.85
20	446.6	935.1		$Nd_2Fe_{14}B_1$ $Nd_{1.1}Fe_4Nd_4$ $NdFe_{12}B_6$	-		0.90

Table 3.5 As table 3.1, but for $(Fe_{0.80}Nd_{0.20})_{100-y}B_y$

y	T_c (K)	T_1 (K)	E_{1a} (ev)	Crystalline Phases	T_2 (K)	Crystalline Phases
5	418.6*	858.5		$Nd_2Fe_{14}B_1$ α-Nd	-	
7.5	418.5	854.8		$Nd_2Fe_{14}B_1$ $Nd_{1.1}Fe_4B_4$ α-Nd	-	
10	425.4	848.0		$Nd_2Fe_{14}B_1$ $Nd_{1.1}Fe_4B_4$ α-Nd	-	
12.5	421.5	863.8	4.05	$Nd_2Fe_{14}B_1$ $Nd_{1.1}Fe_4B_4$ α-Nd	-	
15	413.5	868.1		$Nd_2Fe_{14}B_1$ $Nd_{1.1}Fe_4B_4$ (930K)	970.5	$Nd_2Fe_{14}B_1$ $Nd_{1.1}Fe_4B_4$ α-Nd
17.5	416.3	886.1		$Nd_2Fe_{14}B_1$ $Nd_{1.1}Fe_4B_4$ α-Nd	-	
20	392.9	907.0		$Nd_2Fe_{14}B_1$ $Nd_{1.1}Fe_4B_4$ α-Nd	-	

Table 3.6 As Table 3.1, but for $(Fe_{0.75}Nd_{0.25})_{100-y}B_y$

y	T_c (K)	T_1 (K)	E_{1a} (ev)	Crystalline Phases
5	409.5*	842.2		$Nd_2Fe_{14}B_1$ α-Nd
7.5	406.5	773.6		$Nd_2Fe_{14}B_1$ $Nd_{1.1}Fe_4B_4$ α-Nd
10	402.4	827.2		$Nd_2Fe_{14}B_1$ $Nd_{1.1}Fe_4B_4$ α-Nd
12.5	390.8	834.2	4.3	$Nd_2Fe_{14}B_1$ $Nd_{1.1}Fe_4B_4$ α-Nd
15	381.9	838.9		$Nd_2Fe_{14}B_1$ $Nd_{1.1}Fe_4B_4$ α-Nd
17.5	367.3	847.6		$Nd_2Fe_{14}B_4$ $Nd_{1.1}Fe_4B_4$ α-Nd
20	356.6	858.4		$Nd_2Fe_{14}B_1$ $Nd_{1.1}Fe_4B_4$ α-Nd

Fig. 3.3 The first crystallization temperature (T_1) as a function of the boron concentration for $(Fe_{1-x}Nd_x)_{100-y}B_y$

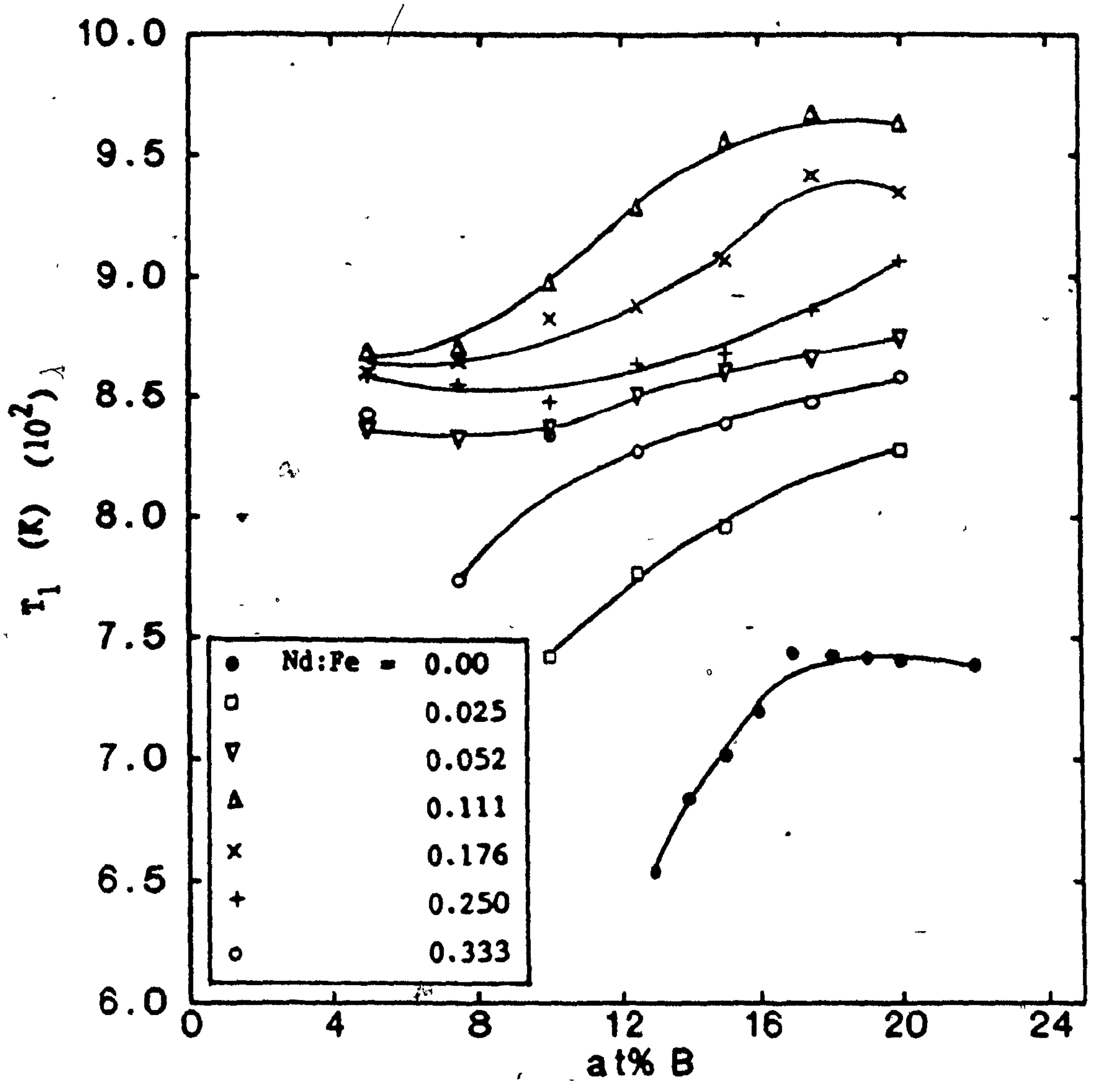

10.0
9.5
9.0
8.5
8.0
7.5
7.0
6.5
6.0
T_1 (K) (10^2)
0
4
8
12
16
20
24
at% B
● Nd:Fe = 0.00
□ 0.025
▽ 0.052
△ 0.111
× 0.176
+ 0.250
○ 0.333

was found in the alloys with Nd:Fe ratio of 0.052. For the alloys with Nd:Fe ratio of 0.052 and 0.333, a linear variation of T_1 with boron was observed with a slope of $\frac{dT}{dy} \approx 3$ (K/at% B). The behaviour of the crystallization temperature with boron content, in the ternary amorphous alloys $(Fe_{1-x}Nd_x)_{100-y}B_y$, is similar to that in binary $Fe_{100-y}B_y$ amorphous alloys. Especially in alloys with Nd:Fe = 0.111 or 0.176, i.e. for boron concentration in the range $12 \leq y \leq 20$, T_1 initially increases rapidly and then slows down slightly at the higher boron concentration. It should be mentioned, however, that all the crystallization temperatures in the ternary system are much higher that in the binary alloys. For example, T_1 is 100K higher in $(Fe_{0.975}Nd_{0.025})_{85}B_{15}$ and 250K higher in $(Fe_{0.90}Nd_{0.10})_{85}B_{15}$ than that for $Fe_{85}B_{15}$ binary alloy.

The more interesting aspect of crystallization is the variation of T_1 with the Nd:Fe ratio as shown in Fig. 3.4. A common feature observed in alloys with different boron concentration is that, initially, T_1 increases sharply with the substitution of iron by neodymium and reaches a peak value at the Nd:Fe ratio slightly higher than 0.111 and then decreases linearly with further additions of neodymium. The enhancement of the crystallization temperature in the range of $0 \leq \frac{Nd}{Fe} \leq 0.111$, is about 250K whereas the reduction of T_1 for $0.111 \leq \frac{Nd}{Fe} \leq 0.333$ is about 100K.

To further study this unusual variation of T_1 with composition, information on crystallization kinetics is required. The activation energy (E_{1a}) corresponding to the first crystallization process for the

Fig. 3.4 The first crystallization temperature (T_1) as a function of the Nd:Fe ratio for $(Fe_{1-x}Nd_x)_{100-y}B_y$

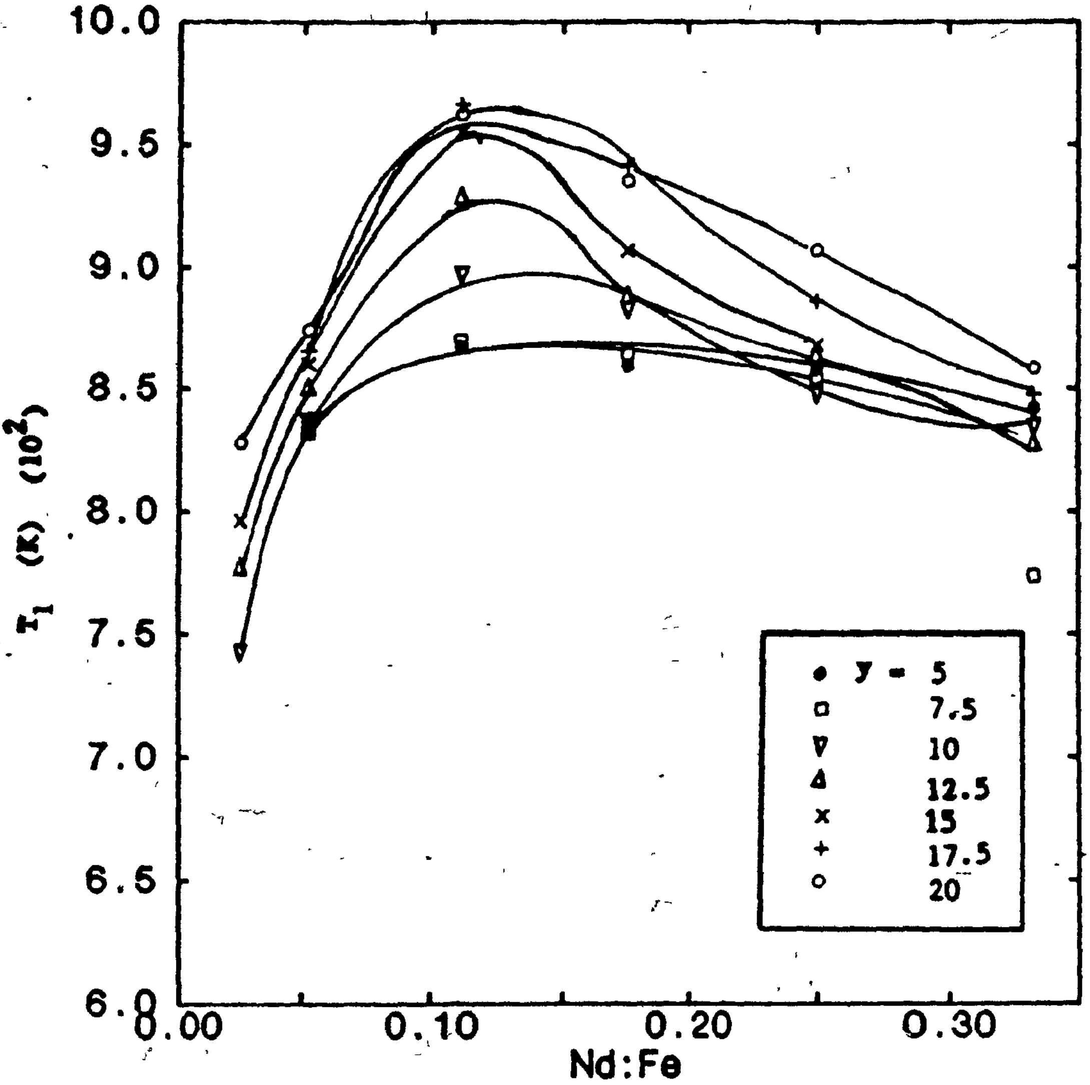
10.0
9.5
9.0
8.5
8.0
7.5
7.0
6.5
6.0
T_1 (K) (10^2)
0.00
0.10
0.20
0.30
Nd:Fe
● y = 5
□ 7.5
▽ 10
△ 12.5
× 15
+ 17.5
○ 20

amorphous alloys $(Fe_{1-x}Nd_x)_{87.5}B_{12.5}$ was determined by the method proposed by Kissinger. Values of E_{1a} of alloys were also listed in tables 3.1 - 3.6. For the sake of examining the correlation between the crystallization temperature (T_1) and corresponding activation energy, we plot T_1 and E_{1a} as a function of the Nd:Fe ratio in Fig.3.5. There is a strong increase of E_{1a} for small Nd:Fe ratios.

It can be concluded from the results presented above that the thermal stability of ternary Nd-Fe-B alloys is proportional to the boron concentration but strongly dependent on Nd:Fe ratio as well. The increase of the crystallization temperature in the binary amorphous alloys of $Fe_{100-y}B_y$ ($13 \leq y \leq 20$) with y is not affected by the substitution of neodymium for iron. The thermal stability, however, in the amorphous Nd-Fe-B ternary alloys is greatly enchanced over that in Fe-B binary amorphous alloys.

The strong dependence of the thermal stability in the ternary amorphous alloys $(Fe_{1-x}Nd_x)_{100-y}B_y$ on the ratio of Nd:Fe, however, is somewhat complicated. In the tables 3.1 - 3.6, the crystalline phases corresponding to the first crystallization products are listed. For alloys with a Nd:Fe ratio of less than 0.111, primary crystallization of α-Fe is the major crystallization product. This mode of crystallization changes, however, to the crystallization of $Nd_2Fe_{14}B_1$ as the major crystalline phase for alloys with Nd:Fe ≥ $0.1\overline{11}$. From the X-ray diagrams, we can clearly see that when the Nd:Fe ratio is increased the amount of primary precipitation

Fig. 3.5 The first crystallization temperature (T_1) and activation energy (E_{1a}) as a function of Nd:Fe ratio for alloys $(Fe_{1-x}Nd_x)_{87.5}B_{12.5}$ ($0.025 \leq x \leq 0.25$)

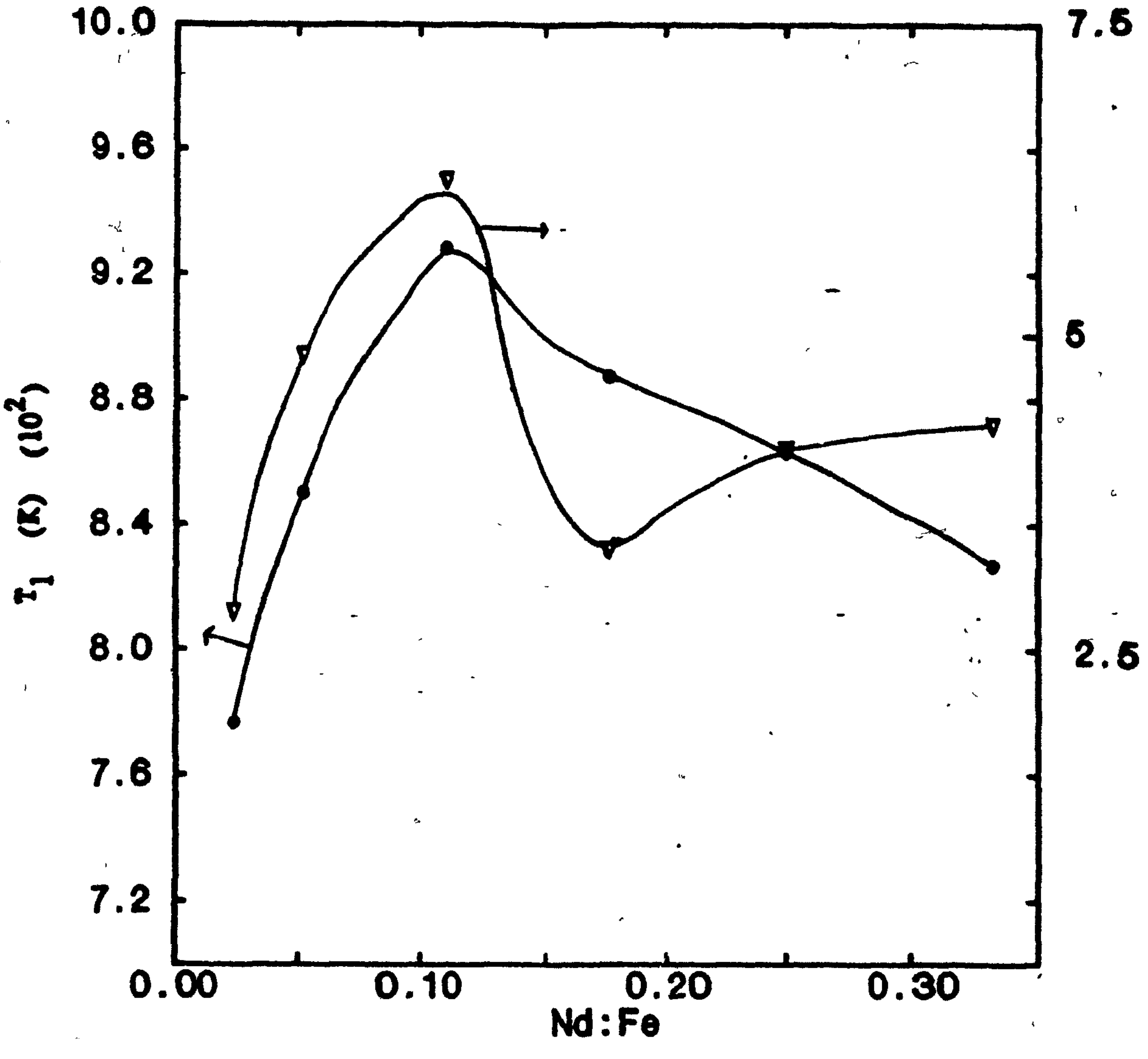
10.0
9.6
9.2
8.8
8.4
8.0
7.6
7.2
T_1 (K) (10^2)
7.5
5
2.5
E_{1a} (ev)
0.00
0.10
0.20
0.30
Nd:Fe

of α-Fe is decreased. This suggests that the strong rise of the crystallization temperature with the addition of small amounts of neodymium is related to the increased stability of the amorphous phase. This is demonstrated by the drastic increase in the activation energy for the formation of α-Fe with the addition of Nd, i.e. with the decrease of the amount of crystallized α-Fe (see Fig. 3.5). The reduction of thermal stability at the higher Nd:Fe ratio and the minimum in E_{1a} at a Nd:Fe ratio of 0.176 is not unexpected. It has been shown <14> that apart from primary crystallization processes, the activation energy for crystallization is lowest for polymorphous crystallization. For $Nd_2Fe_{14}B_1$, the Nd:Fe ratio is 0.143 in qualitative agreement with the experimental data in Fig. 3.5. The appearance of α-Nd observed in crystalline phases for higher Nd:Fe ratio alloys may be responsible for the reduction of crystallization temperature as neodymium content increases.

3.2.2 Crystalline Phases in the Fe-rich Corner of the Ternary Nd-Fe-B System

The crystallization products for the amorphous alloys were determined by heating the samples at the rate of 40 K/min in the DSC up to the highest temperature available 999(K), then cooling it rapidly to room temperature and subsequently examining the structure by X-ray diffraction. The crystalline phases corresponding to certain crystallization exotherms for the alloys were listed in tables 3.1 - 3.6. The regions defining different crystallization modes corresponding to the first crystallization temperature for amorphous Nd-Fe-B alloys are indicated in the Fe-rich corner of Nd-Fe-B phase diagram (see Fig. 3.6). The uncertainties in the position of boundaries is estimated to be less than 2 at%. The equilibrium phases observed in each of amorphous Nd-Fe-B alloys after crystallization are indicated in the Fe-rich corner of the Nd-Fe-B phase diagram shown in Fig 3.7. Fig. 3.8 shows the regions defining different crystallization modes of fully crystallized amorphous Nd-Fe-B alloys. The crystalline phases observed include $Nd_2Fe_{14}B_1$, $Nd_{1.1}Fe_4B_4$, α-Fe, α-Nd, $Nd_2Fe_{23}B_3$, $Nd_1Fe_{12}B_6$ and a new metastable phase. The composition of the new phase is $Nd_6Fe_{128\pm4}B_{17\pm1}$. A detailed discussion of the new metastable phase was made by Altounian et al.<15>. Information on the crystal structures of these phases are included in table 3.7. The phases $Nd_2Fe_{23}B_3$, $NdFe_{12}B_6$ and the new phase $Nd_6Fe_{128\pm4}B_{17\pm1}$ are metastable and it was found from calorimetric measurements that they disappear after annealing in the DSC at 999K for a few minutes. As can be seen in Fig. 3.7, the equilibrium crystalline phases in all the alloys in which the Nd:Fe ratio is greater than 0.175 include α-Nd, $Nd_2Fe_{14}B_1$ and $Nd_{1.1}Fe_4B_4$.

Fig. 3.6 Regions defining different crystallization modes corresponding to the first crystallization temperature of amorphous $(Fe_{1-x}Nd_x)_{100-y}B_y$ alloys. The primary crystallization products observed in each of these regions (a - n) are specified below. Full circles denote equilibrium phases while open circles indicate metastable phases.

a. α-Fe, $Nd_{1.1}Fe_4B_4$

b. α-Fe

c. α-Fe, Fe_3B

d. $Nd_6Fe_{128\pm4}B_{17\pm1}$, α-Fe

e. α-Fe, $Nd_2Fe_{14}B_1$

f. $Nd_2Fe_{14}B_1$, $Nd_2Fe_{23}B_3$, $Nd_{1.1}Fe_4B_4$

g. $Nd_2Fe_{14}B_1$, $Nd_2Fe_{23}B_3$

h. α-Fe, $Nd_{1.1}Fe_4b_4$, $Nd_2Fe_{14}B_1$

i. $Nd_2Fe_{14}B_1$, $Nd_{1.1}Fe_4B_4$, $NdFe_{12}B_6$

j. $Nd_2Fe_{14}B_1$, $Nd_{1.1}Fe_4B_4$

k. $Nd_2Fe_{14}B_1$

l. α-Fe, $Nd_2Fe_{14}B_1$, α-Nd

m. $Nd_2Fe_{14}B_1$, $Nd_{1.1}Fe_4B_4$, α-Nd

n. $Nd_2Fe_{14}B_1$, α-Nd

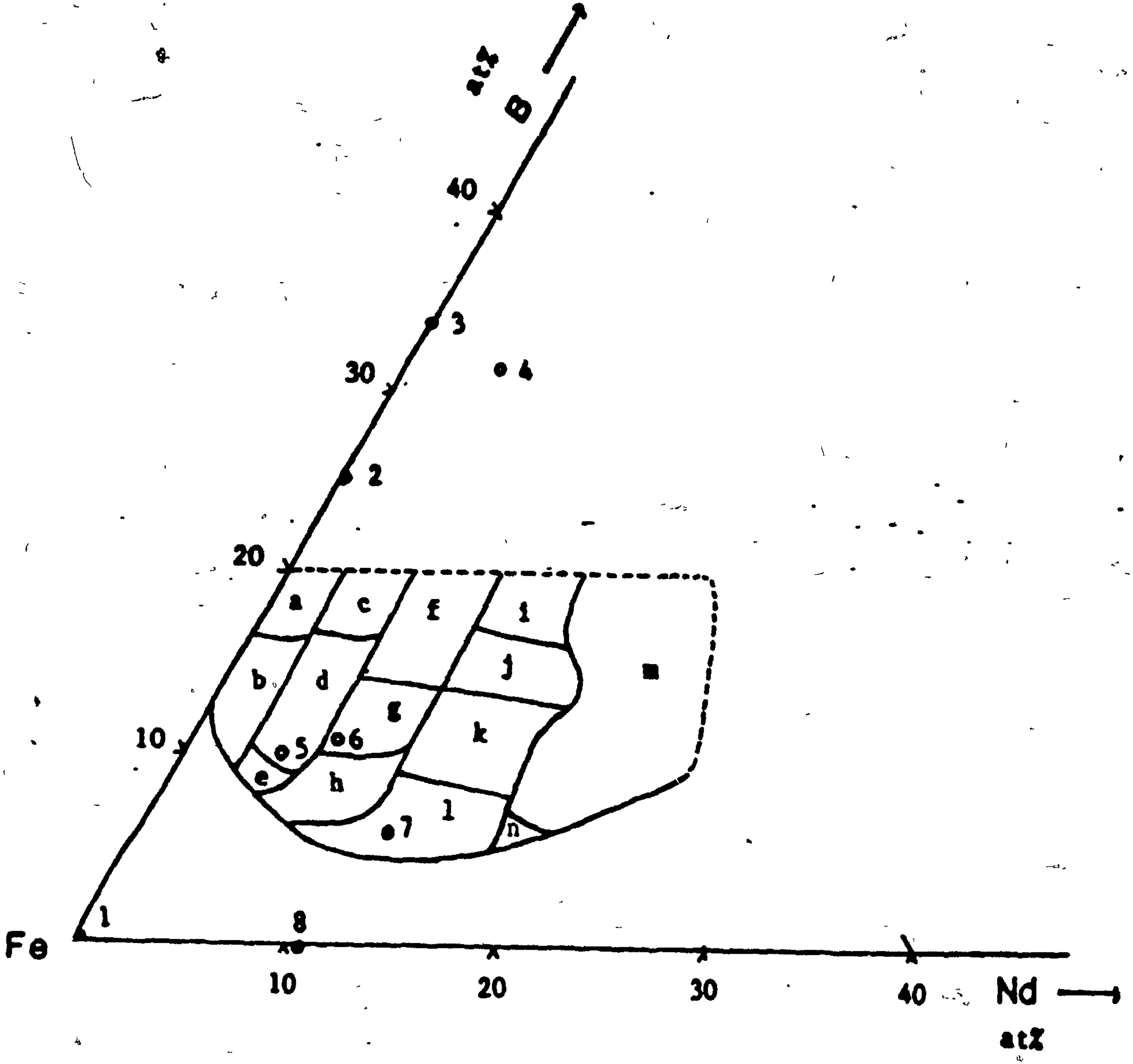

1 - α-Fe

2 - Fe_3B

3 - Fe_2B

4 - $NdFe_{12}B_6$

5 - $Nd_6Fe_{128\pm4}B_{17\pm1}$

6 - $Nd_2Fe_{23}B_3$

7 - $Nd_2Fe_{14}B_1$

8 - Nd_2Fe_{17}

Fig. 3.7 Regions defining different crystallization modes of fully crystallized (1000K) amorphous $(Fe_{1-x}Nd_x)_{100-y}B_y$ alloys. Solid lines correspond to the equilibrium phases while dash lines correspond to the intermediate phases.

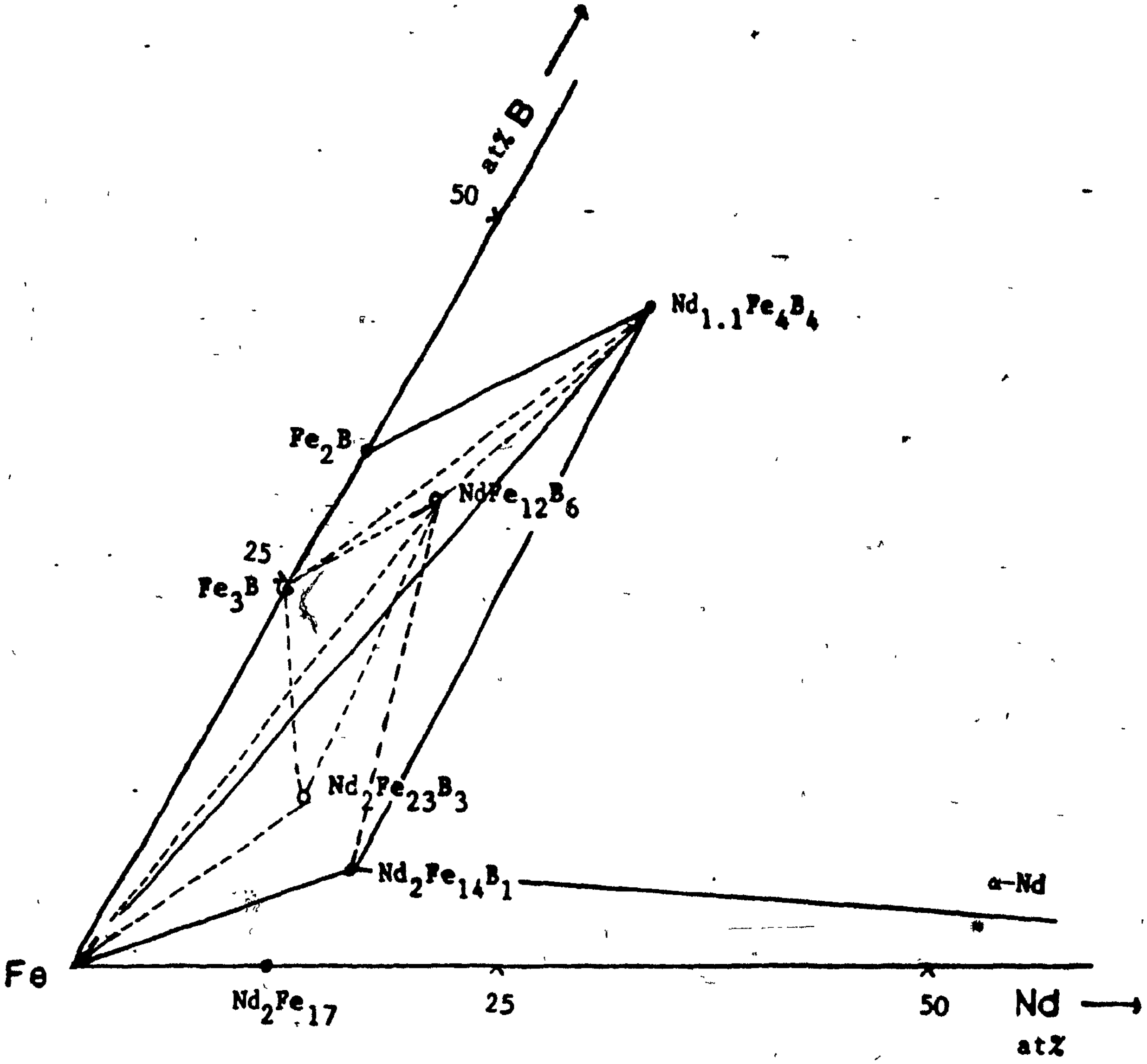
at% B
50
25
Nd$_{1.1}$Fe$_4$B$_4$
Fe$_2$B
NdFe$_{12}$B$_6$
Fe$_3$B
Nd$_2$Fe$_{23}$B$_3$
Nd$_2$Fe$_{14}$B$_1$
α-Nd
Fe
Nd$_2$Fe$_{17}$
25
50
Nd
at%

Table 3.7 Crystal structures of crystalline phases observed in the ternary Nd-Fe-B system.

Crystalline Phases	Structure	Space Group	Lattice Constants
α-Fe	cubic	Im3m	a=0.2866 nm
α-Nd	hexagonal	$P6_3/mmc$	a=0.3658 nm c=1.1797 nm
$Nd_2Fe_{23}B_3$	cubic	$I\bar{4}3d$	a=1.419 nm
$Nd_2Fe_{14}B_1$	tetragonal	$P4_2/mnm$	a=0.8803nm c=1.2196 nm
$Nd_1Fe_{12}B_6$	hexagonal	$R\bar{3}m$	a=0.9605 nm c=0.7549 nm
$Nd_{1.1}Fe_4B_4$	tetragonal	$P4_2/n$	a=0.7117nm c=3.507 nm
$Nd_6Fe_{128\pm4}B_{17\pm1}$	cubic	I*3*	a=1.238 nm

3.3 Magnetic Properties of Amorphous $(Fe_{1-x}Nd_x)_{100-y}B_y$ Alloys

3.3.1 Concentration Dependence of Curie Temperature for Amorphous $(Fe_{1-x}Nd_x)_{1-y}B_y$ alloys

The Curie temperature , T_c, was determined by heating the amorphous samples in the DSC under a flow of oxygen-free argon gas at a rate of 80 K/min. Values of T_c for all amorphous $(Fe_{1-x}Nd_x)_{100-y}B_y$ alloys are included in tables 3.1 - 3.6.

Fig. 3.8 shows the Curie temperature for ternary amorphous alloys as a function of boron concentration. The results of T_c for $Fe_{100-y}B_y$ are taken from Altounian <16>. It can be derived from Fig. 3.8 that the effect of boron content on T_c is strongly dependent on the Nd:Fe ratio. With increaseing Nd:Fe ratio, the increase in T_c with boron content is gradually diminished and for Nd:Fe > 0.176, even a decrease of T_c with increasing boron content is observed. Fig. 3.9 summarizes this variation in T_c where the average slope, $\frac{dT_c}{dy}$, where y is the boron content, is plotted as a function of the Nd:Fe ratio. The values of $\frac{dT_c}{dy}$ (K/at% B) were calculated assuming a linear relation between T_c and boron content. It is apparent that there is a region, where the Nd:Fe ratio is between 0.175 and 0.225, for which the Curie temperature for the ternary amorphous alloys $(Fe_{1-x}Nd_x)_{100-y}B_y$ is independent of the boron concentration in the range of

Fig. 3.8 Curie temperature (T_c) as a function of boron concentration for amorphous alloys $(Fe_{1-x}Nd_x)_{100-y}B_y$

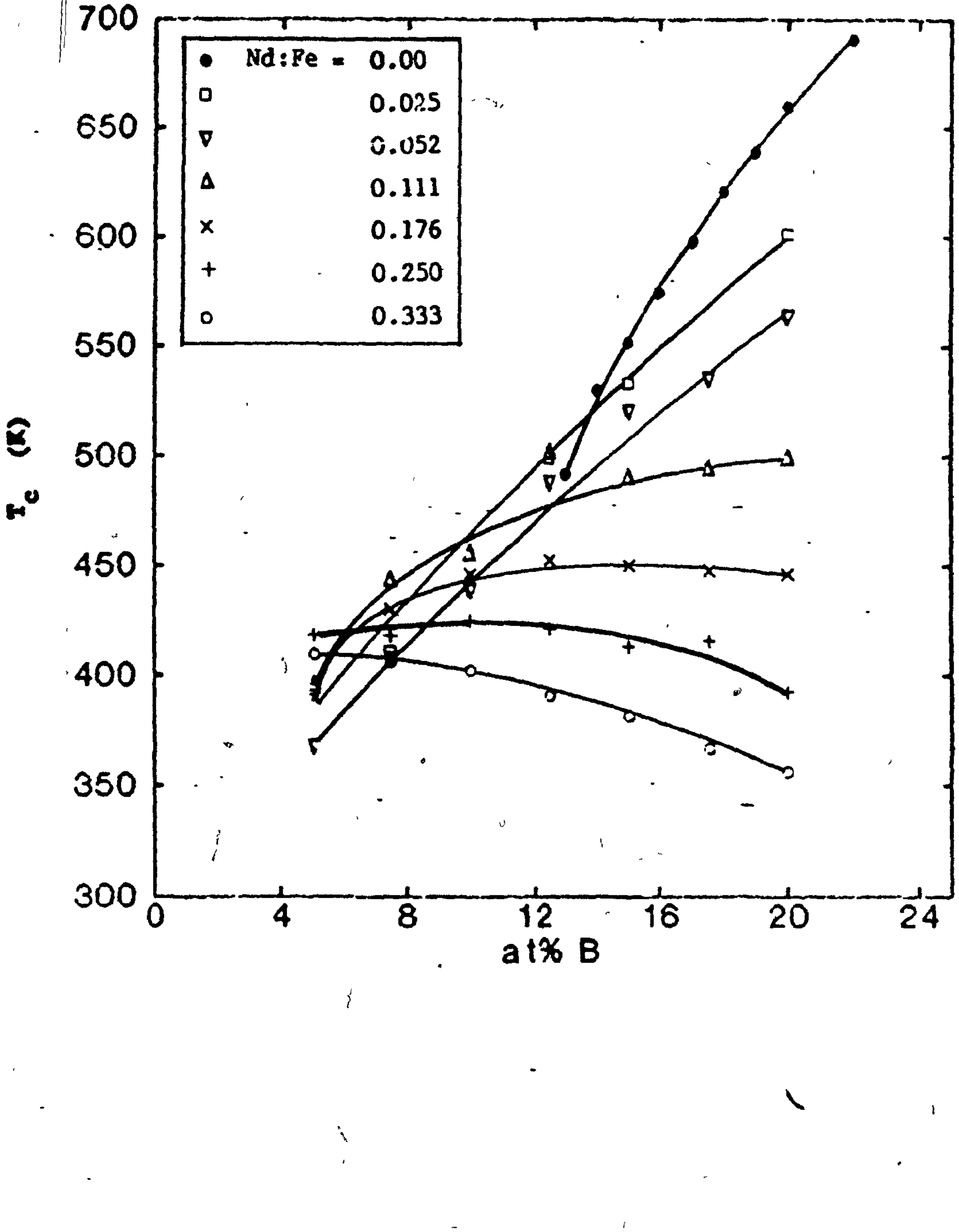

700
650
600
550
500
450
400
350
300
0
4
8
12
16
20
24
at% B
T_c (K)
● Nd:Fe = 0.00
□ 0.025
▽ 0.052
△ 0.111
× 0.176
+ 0.250
○ 0.333

Fig. 3.9 The average slope of Curie temperature (T_c) as a function of boron concentration against Nd:Fe ratio

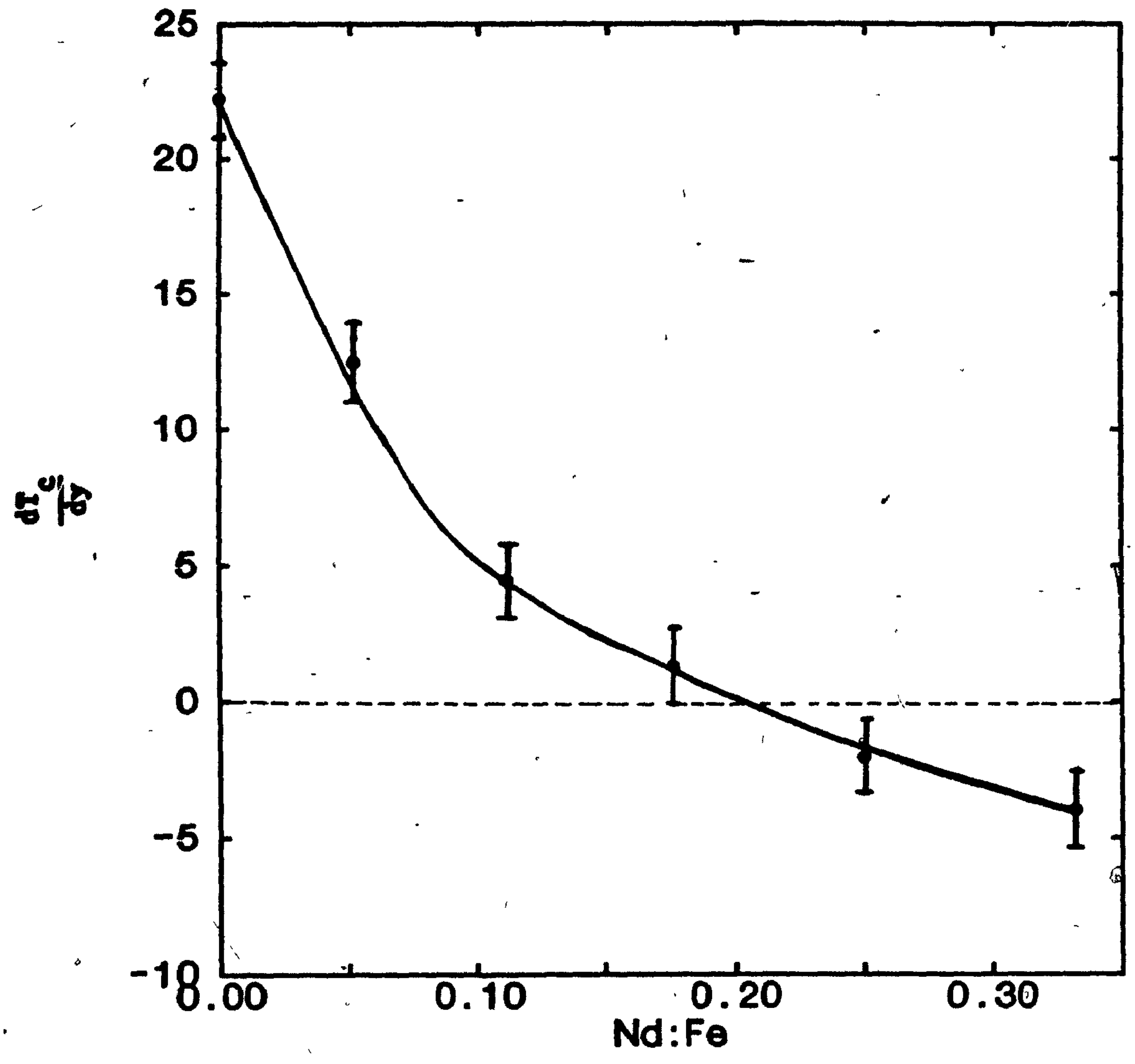

25
20
15
10
5
0
-5
-10
0.00
0.10
0.20
0.30
Nd:Fe
$\frac{dT_c}{dP}$

8 at% $\leq$ B $\leq$ 20 at %. Further research is necessary to understand the origin of this unusual behaviour.

3.3.2 Hard Magnetic Properties of Ternary Nd-Fe-B Alloys

Some of the ternary amorphous Nd-Fe-B alloys were magnetized at room temperature in the VSM with a maxmium available field of 1.7 T before and after crystallization. The values of intrinsic coercive force, ${}_JH_c$, were included in tables 3.3 and 3.4 for the crystallized samples. It was found that the ${}_JH_c$ is very low ($\mu_0{}_JH_c \sim 0.018$T) for amorphous Nd-Fe-B alloys whereas ${}_JH_c$ increased for all the recrystallized alloys. The crystallized alloys with Nd:Fe < 0.176 exhibited soft magnetic properties ($\mu_0{}_JH_c \sim$ 0.25T) and were easily saturated in an applied field of 1.7 T. This behaviour is due to the presence of α-Fe in the equilibrium crystalline phases for these alloys. Alloys with Nd:Fe $\geq$ 0.176, whose crystallization was free of α-Fe formation, were found to be hard magnetic materials ($\mu_0{}_JH_c$ $\sim$ 1.00T). It should be mentioned that the values of coercivity obtained from the present work are minor loop values and therefore not very reliable because of the limited available field for the VSM.

A further study on the magnetization properties of crystalline ternary Nd-Fe-B alloys is presently being carried out by means of a pulse-field technique, with fields up to 25T. It will be very significant to understand the coercivity mechanism of Nd-Fe-B materials and its relation to the microstructure.

CONCLUSIONS

The glass formation and magneteic properties of $(Fe_{1-x}Nd_x)_{100-y}B_y$ $(0.025 \leq x \leq 0.25,\ 5 \leq y \leq 20)$ have been studied. The glass formation was found possible for Nd-Fe-B alloys with iron content less than 87.5 at%. The results show that increasing neodymium content (≥ 20 at%) or decreasing boron content (≤ 7.5 at%) makes it more difficult to prepare amorphous samples.

The thermal stability of ternary amorphous Nd-Fe-B alloys is proportional to boron concentrations but strongly dependent on Nd:Fe ratio as well. The strong increase of the crystallization temperature with additions of small amounts of neodymium to Fe-B is attributed to the increasing difficulty of α-Fe formation upon crystallization. The reduction of thermal stability at the higher Nd:Fe ratio is due to the polymorphic crystallization of the tetragonal hard magnetic phase $Nd_2Fe_{14}B_1$. Ternary phase diagrams for the initial and final crystallization products were established.

The increase in Curie temperature of amorphous Nd-Fe-B alloys with boron content is gradually diminished as Nd:Fe ratio increases. There is a region, where the Nd:Fe ratio is between 0.175 and 0.225, for which the Curie temperature for amorphous Nd-Fe-B alloys is independent of the boron content in the range of 8 at% ≤ B ≤ 20 at%. For Nd:Fe > 0.176, the Curie temperature decreases with increasing boron content. The intrinsic coercivities of the amorphous Nd-Fe-B alloys was less than 0.018 Tesla for all compositions. After crystallization the coercivities increased by a factor of about 50, specially for alloys free of α-Fe.

REFERENCES

<1> M. Sagawa, S. Fujimura, M. Togawa and Y. Matsuura, J. Appl. Phys. 55 (1984) 2083

<2> J. J. Croat, J. F. Herbst, R. W. Lee and F. E. Pinkerton, J. Appl. Phys. 55 (1984) 2078.

<3> N. C. Koon and B. N. Das, J. Appl. Phys. 55 (1984) 2063

<4> K. H. J. Buschow, Materials Sci. Reports, 1 (1986) 1-64

<5> K. Strnat, G. Hoffer, J. Olson, W.Ostertag and J. J. Becker J. Appl. Phys. 38 (1967) 1001

<6> A. L. Robinson, Science, 223 (March 1984) 920-2

<7> A. E. Clark, Appl. Phys. Letters 23 (1973) 642.

<8> J. J. Croat, IEEE Trans. Magn. MAG-18 (1982) 1442.

<9> J. J. Croat, J. Appl. Phys. 53 (1982) 6932.

<10> P. Duwez, Trans. Am. Soc. Metals, 60 (1967) 607

<11> S. H. Aly, G. N. Nicolaides, Y. F. Tao and G. C. Hadjipanayis, J. Phys. F: Met. Phys. 16 (1986) L21 - L26.

<12> K. H. J. Buschow, D. B. De Mooij and H. M. Van Noort, J. Less - Common Met. 125 (1986) 135.

<13> H. E. Kissinger, Anal. Chem. 29 (1957) 1702

<14> Z. Altounian, Tu. Guo - Hua and J. O. Strom - Olsen, J. Appl. Phys. 54 (1983) 3111.

<15> Z. Altounian, D. H. Ryan and G. H. Tu, The 4th

Joint MMM - Intermag. Conference, Vancouver, B. C, (July 1988)

<16> Z. Altounian, J. O. Strom - Olsen and M. Olivier,
Mat. Res. Soc. Symp. Proc. Vol 58 (1986) 81